




## Viscosity of Pyroxenite Melt and Its Evolution During Cooling

F. Vetere<sup>1,2</sup> , M. Murri<sup>3</sup>, M. Alvaro<sup>3</sup>, M. C. Domeneghetti<sup>3</sup>, S. Rossi<sup>1</sup> , A. Pisello<sup>1</sup>, D. Perugini<sup>1</sup> , and F. Holtz<sup>2</sup>

<sup>1</sup>Department of Physics and Geology, University of Perugia, Perugia, Italy, <sup>2</sup>Institute of Mineralogy, Leibniz Universität Hannover, Hannover, Germany, <sup>3</sup>Department of Earth and Environmental Sciences, University of Pavia, Pavia, Italy

### Key Points:

- New viscosity data under controlled cooling and shear rates for a pyroxenite, analog of Martian nakhlites, are presented
- Changes in apparent viscosity behavior are observed with a decrease of viscosity of approximately 1 log unit between two different experiments as shear rate ( $\dot{\gamma}$ ) varies from 0.1 to 1.0 s<sup>-1</sup>
- Lava flow capability and crystallization dynamics are discussed in the framework of possible scenarios occurring on Earth and on Mars

### Supporting Information:

- Supporting Information S1
- Figure S1
- Figure S2
- Figure S3
- Table S1
- Table S2
- Table S3
- Table S4
- Table S5
- Table S6

### Correspondence to:

F. Vetere,  
francesco.vetere@unipg.it

### Citation:

Vetere, F., Murri, M., Alvaro, M., Domeneghetti, M. C., Rossi, S., Pisello, A., et al. (2019). Viscosity of pyroxenite melt and its evolution during cooling. *Journal of Geophysical Research: Planets*, 124. <https://doi.org/10.1029/2018JE005851>

Received 16 OCT 2018

Accepted 23 APR 2019

Accepted article online 2 MAY 2019

**Abstract** New viscosity experiments at superliquidus temperatures and during cooling at a rate of 10 K/hr have been performed at different shear rates on a synthetic pyroxenite melt. Results revealed that this melt is extremely fluid at temperature between 1646 and 1530 K and measured viscosities are between 2.2 and 7.8 Pa·s. Such very low viscosities allow the lava to flow in turbulent regime as confirmed by the high Reynolds numbers, which are always >2,000. As a consequence, very long distance could be covered by the lava flow. If we consider this studied composition as proxy for Mars lava flows coupled with very high effusion rates, our results might explain the presence of extraordinary large volcanic channels, as recently hypothesized for the Kasei Valles on Mars, even considering that the gravity is approximately one third that of Earth. Few literature data tracking viscosity during cooling are available, and they reported shear thinning effect on different compositions. Our experiments performed at 0.1 and 1 s<sup>-1</sup> have shown complex variation in the apparent viscosity, confirming that nonequilibrium rheology represents a still unexplored field of investigation useful to better understand the real geological scenarios occurring in magmatic and volcanic systems.

**Plain Language Summary** The study of the flow of matter (rheology) is the key factor to understand dynamic processes and behavior of magma rising through volcanic conduit and lava emplacement on Earth or other terrestrial planets. Today we can monitor the evolution of magma and volcanic mixtures by measuring their viscosity and its variation as temperature, composition, and fluid regimes vary. The available data are mainly derived from isothermal experimental approaches, and very few studies focused on monitoring viscosity behavior while changing both the cooling rate and the shear stress. In this study we have monitored in detail the viscosity variation of an analog composition prepared to reproduce Theo's Flow lava (Ontario, CA), considered as a terrestrial analog of Martian nakhlites. Measurements were performed using the concentric cylinder technique. Results show a very high fluidity of the melt in the temperature range between 1643 and 1530 K (2.2 to 7.8 Pa·s). As temperature drops into the subliquidus temperature (i.e., below 1530 K), apparent viscosity continuously increases to 6 × 10<sup>4</sup> Pa·s, where a brittle failure was observed. These results can provide indications on how extraordinary long lava flows might have developed on the Martian surface.

## 1. Introduction

Recently, experiments under constant temperature were performed in order to study the behavior of lavas in different geological settings on both Earth and other Earth-like planets (Chevrel et al., 2013; Rossi et al., 2017; Sehlke & Whittington, 2015; Vona et al., 2011, and references therein). Indeed, volcanic eruptive styles are governed by magma rheology, and rheology governs lava emplacement mechanisms. Most of the published experimental approaches aim to track the viscosity variation as a function of temperature, volatile content, and crystallinity. Moreover, experimental study on crystallization induced by variable decompression rates allowed scientists to shed new light on processes governing magma ascent dynamics (Fiege et al., 2015, and references therein). Following the pioneering work of Carmichael (1974), reporting the rheological importance of the coexistence of crystals and liquid material, melt solidification processes have been investigated via experiments under different applied cooling rates (see Hammer, 2008, for a general summary). Diverse studies at crystal-melt disequilibrium conditions have been performed (e.g., Lofgren, 1980; Cashman, 1993; Lange et al., 1994; Arzilli & Carroll, 2013; Vetere et al., 2015, and reference therein), but only recently has even the deformation acting on lavas been taken into account with both laboratory

approaches (Kolzenburg et al., 2018; Kolzenburg et al., 2018; Kolzenburg et al., 2019) and direct measurements in the field (Chevrel et al., 2018). These are extremely important mechanisms that deserve further investigation as most of the magmatic and volcanic environment are controlled by nonequilibrium processes. Magma or lava rheology changes over time, even if imposed variables such as composition and temperature remain the same.

In this contribution, we present new results about the role of shear rates on the viscosity of partly crystallized silicate melts and an attempt to link different shear rates to nucleation and growth timescales (Kolzenburg et al., 2016) collecting viscosity data under a controlled cooling rate.

As stated in the review provided by Wilson and Head (1994), the “full range of volcanic eruption styles observed on Earth is to be expected” on Mars as well. “Due to the lower gravity, fluid convective motions and crystal settling processes will be slower on Mars than on Earth, and this fact guarantees larger diapirs to ascend to shallower depths. Thus, it is plausible that the dike widths increase on Mars by a factor of 2 and this results on higher effusion rates estimated by a factor of 5. The lower gravity causes cooling-limited flows to be longer, implying that we might expect compositionally similar cooling-limited lava flows to be about 6 times longer on Mars than on Earth.” As a consequence, as reported in Wilson and Head (1994), Icelandic Laki lava flows (30–60 km in length) would have 200–350 km of length on Mars.

In this context, caution must be taken on the effect of gravity and cooling on Mars compared to Earth, by considering identical volume and topography. Thus, this would provide a potential explanation for the several hundreds of kilometers of flows that have been documented on the Martian surface (Kasei Valles or the more recently debated Hrad Vallis; Hopper & Leverington, 2014; Leverington, 2018). In particular, Kasei Valles is considered to be the largest outflow system on Mars with a length of more than 2,000 km and a width of up to several hundred kilometers. The total volume of magma erupted is estimated to be  $\sim 5 \times 10^6 \text{ km}^3$  and, in magnitude, is comparable to some of the large igneous provinces on Earth like the Deccan Traps with an area of  $0.5\text{--}1.5 \times 10^6 \text{ km}^2$  and a volume estimate of  $>1.5 \times 10^6 \text{ km}^3$  (Coffin & Eldholm, 1994).

On the other hand, we can only refer to lava rheology estimates derived from remote sensing data, which are actually one of the most applied methods, to retrieve lava flow velocity (e.g., Hulme, 1974; Moore et al., 1978; Hiesinger et al., 2007; Chevrel, Giordano, et al., 2013). This methodology considers morphologic similarities between terrains on terrestrial planets and those observed on Earth. In fact, the emplacement of lava flows can be modeled using a single rheological parameter (apparent viscosity or apparent yield strength) calculated from morphological dimensions by using Jeffreys' and Hulme's equations (Jeffreys, 1925; Hulme, 1974).

Nonetheless, given the nonlinear dynamics of lava flows and domes, which may determine remarkable thermal effects, significant limitations may be observed and should be carefully considered before applying this method to any natural context (Giordano, 2019, and reference therein).

Being aware that there are only few studies that tried to quantify the lava rheology of Martian volcanism (Chevrel et al., 2013; Chevrel et al., 2014; Sehlke & Whittington, 2016; Vaucher et al., 2009; Wilson et al., 2009; Wilson & Head, 1994) and considering that the composition investigated in this study is similar to Martian nakhlites (see Table 1), we used our new viscosity data to estimate the lava flowing ability of one of the potential volcanic compositions erupted on Mars.

Sehlke and Whittington (2016) provided new methods for the estimation of the viscosity of planetary tholeiitic melts, pointing to model various volcanic processes, while Dundas and Keszthelyi (2014) calculated emplacement and (thermal) erosive effects of lava in south Kasei Valles on Mars. In both approaches, temperature and melt composition are required in order to calculate viscosity and estimate the lava flow velocity and lava flux. To our knowledge, only very few experimental data sets on planetary magma/lava viscosity introduce cooling rate and shear rates as potential parameters affecting magma mobility (e.g., Kolzenburg et al., 2019; Kolzenburg, Giordano, et al., 2018). Presently, only a few general models and combined equations (e.g., Mader et al., 2013; Vona et al., 2011) are able to track viscosity variation taking into account the crystalline phases in terms of their volume, aspect ratio, and applied shear stress. However, most existing viscosity models are not very accurate when applied to compositions that are different from those used in the experiments. The aim of this work is to better understand the rheology of multiphase silicate melt systems

**Table 1**  
Compositions of Residual Glasses of the Crystal-Bearing Run Products and of the Starting Material

	SiO <sub>2</sub> (wt %)	TiO <sub>2</sub> (wt %)	Al <sub>2</sub> O <sub>3</sub> (wt %)	FeO (wt %)	MgO (wt %)	CaO (wt %)	Na <sub>2</sub> O (wt %)	K <sub>2</sub> O (wt %)	Fe <sup>2+</sup> /Fe <sub>tot</sub> (wt %)	$\rho$ (kg/m <sup>3</sup> )	NBO/ T (F)	$\Phi_{tot}$ (vol-area %)	$\Phi_{Cpx}$ (vol-area %)	$\Phi_{Ol}$ (vol-area %)	$\Phi_{Ox}$ (vol-area %)
SM	51.97	0.79	5.82	10.63	14.41	15.16	1.11	0.12	0.22	2.774 <sup>a</sup>	1.14 <sup>c</sup>	0	0	0	0
std	0.30	0.03	0.15	0.23	0.36	0.22	0.04	0.02	0.02	2.698 <sup>b</sup>	0.73 <sup>d</sup>				
TF0.1-1	55.78	1.63	11.48	11.00	7.00	10.26	2.46	0.23	0.16	2.670 <sup>a</sup>	0.48 <sup>c</sup>	62.6 <sup>f</sup>			
std	0.73	0.06	0.44	0.81	0.31	0.39	0.21	0.02	0.02	2.605 <sup>b</sup>	0.58 <sup>e</sup>	65.4 ± 7.3 <sup>g</sup>	60.5 ± 7.1 <sup>g</sup>	2.9 ± 0.8 <sup>g</sup>	1.8 ± 0.5 <sup>g</sup>
TF0.1-2	51.52	1.18	9.01	14.51	10.02	11.58	1.90	0.20	0.20	2762 <sup>a</sup>	0.73 <sup>c</sup>	51.2 <sup>f</sup>			
std	0.29	0.02	0.15	0.16	0.16	0.20	0.06	0.02	0.01	2.689 <sup>b</sup>	0.64 <sup>e</sup>	50.5 ± 6.3 <sup>g</sup>	47.2 ± 5.8 <sup>g</sup>	1.8 ± 0.7 <sup>g</sup>	1.5 ± 0.5 <sup>g</sup>
TF1-1	53.66	1.25	9.77	12.50	8.87	11.59	2.00	0.22	0.18	2.719 <sup>a</sup>	0.65 <sup>c</sup>	53.1 <sup>f</sup>			
std	0.56	0.04	0.13	0.58	0.20	0.23	0.06	0.01	0.02	2.650 <sup>b</sup>	0.63 <sup>e</sup>	49.3 ± 5.7 <sup>g</sup>	47.4 ± 5.0 <sup>g</sup>	0 <sup>g</sup>	1.9 ± 0.8 <sup>g</sup>
Nakhla	48.84	0.34	1.61	19.69	12.93	14.85	0.46	0.14							
Th top 120	49.74	1.04	8.57	15.93	11.92	11.41	1.11	0.05							
Th per 6.9	44.11	0.50	4.03	15.83	32.96	2.46	0.03	0.01							
Th per 10.1	44.52	0.46	3.73	15.85	30.93	4.26	0.02	0.02							
Th pxite 32.4	52.53	0.71	5.46	11.16	13.97	15.47	0.29	nd							
Th pxite 51.9	52.40	0.79	6.09	11.54	13.21	14.93	0.78	nd							

*Note.* The starting composition (SM) as well as experimental residual glass compositions (TF0.1-1, TF0.1-2, and TF1-1) represent an average of 20 measurements. Results are reported in wt %. std refers to 1 standard deviation. Determination of ferrous-ferric ratios was achieved by a wet chemical microcolorimetric method (Schuessler et al., 2008; Vetere et al., 2014). Comparison with natural compositions from Nakhla and Theo's Flow (see Lentz et al., 1999) is also reported. nd = no data.

<sup>a</sup>Glass density was estimated using the model of Klöb (2000) adding 0.02 wt % H<sub>2</sub>O. <sup>b</sup>Melt density was calculated using the Ochs and Lange (1999) model at 1573 K and adding water content equal to 0.02 wt %. <sup>c</sup>The nonbridging oxygen per tetrahedron (NBO/T) values as reported in Mysen and Richet (2005) and Mysen et al. (1982) were calculated by considering the reported Fe<sup>2+</sup>/Fe<sub>tot</sub> ratios. <sup>d</sup>SM fragility is calculated by using Vogel-Fulcher-Tammann parameters (see equation 3 and related parameters) following Angell (1985),  $F = B/(T_g \times (1 - T_0/T_g)^2)$ . <sup>e</sup>For experimental compositions TF0.1-1, TF0.1-2, and TF1-1, Vogel-Fulcher-Tammann parameters were estimated according to the Giordano et al. (2008) general model. <sup>f</sup>Mass balance calculation. <sup>g</sup>Image analyses data.

with the hope that such data could be incorporated into a general model able to track magma/lava rise and flow before emplacement. Up to now, such experiments have been performed under isothermal conditions and, in some cases, at variable shear rates (Sato, 2005; Ishibashi & Sato, 2007; Caricchi et al., 2007; Ishibashi, 2009; Vona et al., 2011, Vona & Romano, 2013; Pistone et al., 2012; Mader et al., 2013, and reference therein; Sehlke & Whittington, 2015; Campagnola et al., 2016; Vetere et al., 2017). Recently, Kolzenburg et al. (2017), following the work of Giordano et al. (2007), highlighted the importance of monitoring the viscosity during cooling, suggesting that it is an important influence also of the applied shear rates. Data from Kolzenburg et al. (2017) and Kolzenburg, Di Genova, et al., 2018, Kolzenburg, Giordano, et al., 2018, Kolzenburg et al., 2019) show that the effective viscosity of the lava can drastically increase, as a function of temperature and time, until reaching a specific subliquidus temperature that, revising the concept first introduced by Giordano et al. (2007), they named  $T_{cutoff}$  suggesting that the viscosity increase is a consequence of the onset of crystallization, which is mainly controlled by the cooling rate. In such a context these authors also highlighted a second-order shear rate effect on the rheological departure. In this contribution, we present new experimental results complementing the data set of viscosity measurements under controlled cooling and shear rates conditions to investigate the change in viscosity induced by crystal nucleation and growth. We use a pyroxenite melt as a starting material that is representative of the composition of Theo's Flow (Ontario, Canada), already extremely well characterized by Lentz et al. (1999, 2011) and considered a terrestrial analog of Martian nakhilites. The most salient compositional and textural features are reported in Table 1. Furthermore, constraints on mineral cooling rates and closure temperatures for the system of Theo's Flow were already available in Alvaro et al. (2015) and in Murri et al. (2016) where the authors estimated a cooling rate of about 0.091 K/hr for a lava flow of 50 m in thickness and a  $T_C$  value around 973 K for clinopyroxenes (augites). The intracrystalline geothermometry was then validated against synthetic augite crystals in Murri et al. (2018) where the authors measured

closure temperatures nearly identical with respect to the quenching temperatures of the experiments. These constraints on the natural samples provide background parameters to be used for our controlled laboratory experiments.

## 2. Starting Material

A synthetic composition derived from a pyroxenite from Theo's Flow is used to test shear rate effects on crystal nucleation and growth during cooling. Theo's Flow lava, located in the Munro Township, eastern Ontario, is described as a differentiated, 120-m-thick lava flow containing peridotite, clinopyroxenite, and gabbro layers covered by hyaloclastite at the top (Lentz et al., 1999, 2011). This lava flow dates to the Archean age (approximately 2.7 Ga) on the basis of the age determined at nearby komatiites (Shirey, 1997). Its name was attributed by Arndt (1977), who first identified and described it. Hyaloclastite at the top quenched margin is a breccia that probably suggests, together with pillow basalts and pyroclastics that occur in this area, a subaerial and/or shallow submarine origin for Theo's Flow (Condie, 1981). Details on the geological setting are reported in Lentz et al. (2011, and references therein). Due to its compositional similarity to nakhlites, one of the most known Martian meteorite groups, this flow is of potential relevant scientific interest also for the study of volcanism on other terrestrial bodies (Friedman, 1998).

The starting material was prepared by melting a mixture of oxides and carbonates. Melting was performed in a Nabertherm HT 04/17 MoSi<sub>2</sub>-heated box furnace (Nabertherm GmbH, Lilienthal, Germany) at 1673 K, in air. Then, the melt was rapidly quenched to glass by pouring it on a brass plate. As proved by subsequent Raman spectroscopy analysis on quenched glass (see supporting information Figure S1), the adopted quenching rate allows us to get homogeneous glass, avoiding the occurrence of quench crystals (Vetere et al., 2015, 2017). Qualitatively, the synthetic composition of Theo's Flow shows very high fluidity during quenching, suggesting a high ability to flow.

## 3. Analytical and Experimental Methods

Chemical compositions for the starting material and run products were determined by using the electron probe microanalyses (EPMA) installed at the Department of Mineralogy at the University of Hannover (DE), following the procedure reported in Rossi et al. (2017) for glasses and in Vetere et al. (2017) for crystalline phases. Table 1 shows the starting compositions presented in this study plus densities calculated according to Ochs and Lange (1999) for melts and Klöß (2000) for glasses. Nonbridging oxygen per tetrahedron was calculated following the method described in Mysen et al. (1982), considering Fe<sub>2</sub>O<sub>3</sub> as a network former and FeO as a network modifier (Table 1). The determination of ferrous-ferric ratios was achieved by a wet chemical microcolorimetric method as proposed in Schuessler et al. (2008) and Vetere et al. (2014).

A rotational Anton Paar RheolabQC viscometer head, equipped with a Gero HTRV 70-250/18 high-temperature tube furnace, was used to measure viscosity. This apparatus is installed at the Petro-Volcanology Research Group labs at the University of Perugia and can operate up to 2073 K at room pressure. A Pt<sub>80</sub>-Rh<sub>20</sub> crucible with an inner radius of 18.5 mm, an outer radius of 20 mm, and a height of 70 mm was used to host the silicate melt. The spindle is made of Al<sub>2</sub>O<sub>3</sub> (with a diameter of 12.2 mm and a length of 60 cm) and is fixed to the head of the viscometer by a standard collet chuck. In order to avoid any contamination of the silicate melts during the experimental runs, the spindle's lower end is covered by a tight-fitting 0.2-mm-thick Pt<sub>80</sub>-Rh<sub>20</sub> foil. An Al<sub>2</sub>O<sub>3</sub> cylindrical pin (2 mm in diameter and 15 mm in length) is inserted in the previously drilled spindle stabilizing the Pt<sub>80</sub>-Rh<sub>20</sub> cover. The rotational viscometer allows measurements under controlled shear rate ( $\dot{\gamma}$ ) and can be used to investigate possible shear effects on the viscosity of melts or partly crystallized systems. Methods and procedures described by Ishibashi (2009) were applied in order to determine melt viscosity. For viscosities of assemblages composed of melt + crystals we followed the same procedure as in Kolzenburg et al. (2016). Briefly, principles of the concentric cylinder rotational viscometer consider that the molten sample is standing in the gap separating the fixed outer cylinder from the rotating inner cylinder run at constant angular velocity ( $\Omega$ ). Krieger and Elrod (1953) and Spera et al. (1988) have shown that  $\Omega$  is related to the shear stress ( $\sigma$ ) by the following relation:

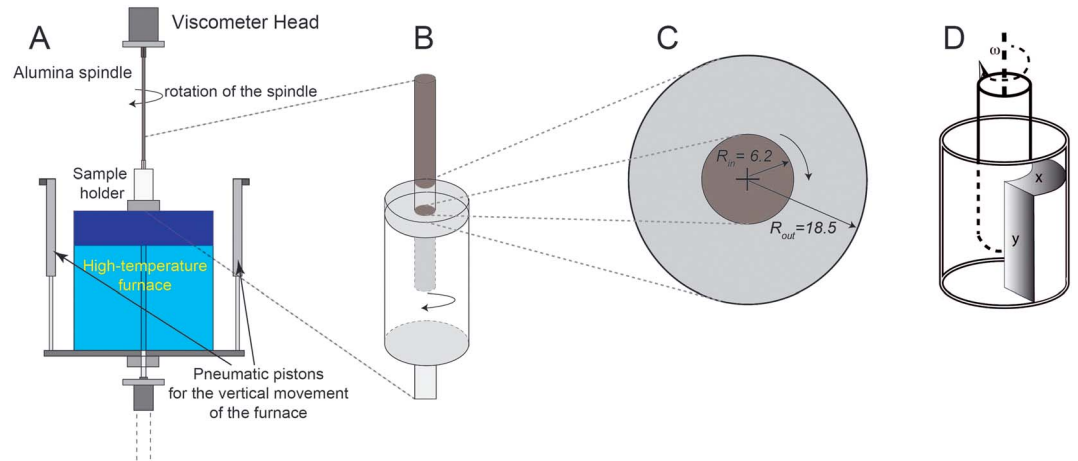


**Figure 1.** Details of the furnace, viscometer, and sample holder used in this work. Note (a) the movable furnace, (b) the Al spindle covered with Pt cup, and (c) the size of the spindle and the crucible. (d) Details of the sample sections used for the analytical and textural analyses (see text).  $x$  and  $y$  are, respectively, perpendicular and parallel cut sections of the sample relative to the spindle.

$$\Omega = \frac{1}{2} \int_{\sigma_c}^{\sigma_i} \dot{\gamma} d\sigma \quad (1)$$

where  $\sigma_i$  and  $\sigma_c$  are the shear stresses at the surfaces of the inner and outer cylinder, respectively. In addition, the relation between the rotational torque ( $\tau$ ) and  $\sigma$  at a distance  $r$  from the rotational axis can be described as follows:

$$\tau = 2\pi hr2\sigma \quad (2)$$

where  $h$  is the length of the inner cylinder immersed in a molten sample.

For the instruments used in this study, the maximum torque is quantified to be between 0.2 and 75 mNm. This would correspond to a viscosity range varying between 0.1 and  $10^8$  Pa·s.

Consequently, data collected at the low torque end have larger relative uncertainties.

In our case, to measure melt viscosity, we performed measurements at shear rates up to  $20 \text{ s}^{-1}$  (see section 4), while for the subliquidus measurements shear rates were 1 and  $0.1 \text{ s}^{-1}$  (details of the measurements are reported also in the supporting information).

As reported above, Theo's Flow was expected to have a high ability to flow at high temperature. Thus, before running experiments, we calibrated the viscometer using a Wacker silicone standard having a viscosity of 10 Pa·s (Spina et al., 2016). One hundred measurements were performed at 298 K, and the results showed good reproducibility, with average values of  $9.8 \pm 0.3$  Pa·s. Moreover, a second calibration was performed by using NIST 717a standard glass, for which the temperature-viscosity relationship is accurately known (<https://www.nist.gov>). Reproducibility of measurements on the standard glass is on the order of  $\pm 0.03$  log unit.

The furnace can move vertically using two pneumatic cylinders (details are reported in Figure 1). For further details on the experimental setup please refer to Morgavi et al. (2015). Temperature was monitored using an in-house built S-type thermocouples (Pt<sub>10</sub>Rh<sub>90</sub> versus Pt) within an Al<sub>2</sub>O<sub>3</sub> sheath, placed inside the spindle and at the bottom of the crucible. As the rotation of the viscometer prevents the use of thermocouples directly wired to a controller, OMEGA wireless thermocouple transmitters UWTC-Series were employed (OMEGA Engineering, Inc., Stamford, CT, USA). Uncertainty on temperature measurements is on the order of 1 K. Following the calibration proposed by Kolzenburg et al. (2016), one or several wireless thermocouples were positioned inside the spindle, and the accuracy of the temperature reading was  $\pm 1$  K. We also find a stable thermal gradient, but since our experiments are run at a relatively high temperature (1673–1473 K), this thermal gradient is  $< 2$  K, in agreement with Kolzenburg et al. (2016).

Prior to viscosity measurements, approximately 70 g of melt was stirred at 1673 K for 2 hr at strain rates of 5–20 s<sup>-1</sup>. This procedure causes the complete removal of gas bubbles and the attainment of a compositionally homogeneous melt (Iezzi et al., 2011; Vetere et al., 2013, 2015). Each melt viscosity experiment has to be considered as a single experiment since after collecting viscosity data, we quenched it and the next experiment was restarted at superliquidus conditions.

Samples used in the subliquidus temperature experiments were first melted at superliquidus conditions. At the end of the experiments, samples were quenched by moving the spindle + crucible into the cooled head of the furnace. The initial quench rate was of the order of approximately 7000 K/hr, which was sufficient to avoid the formation of quench crystals. After quenching, run products were drilled out from the crucible using a diamond core drill and then were mounted in epoxy, ground flat and polished for textural and chemical analyses. The phase compositions, that is, starting melts, glass matrix, and crystalline phases, of all run products were carried out by using EPMA. The analytical conditions of EPMA were the same as those reported in Vetere et al. (2017).

Backscattered electron (hereafter BSE) images were collected by field emission scanning electron microscopy (FE-SEM; FEG LEO 1525, Zeiss Company, Germany) at the Department of Physics and Geology of the University of Perugia (Italy). The energy dispersion X-ray spectroscopy analysis (Quantax 200 with an Xflash 400 detector, Bruker Company, Germany), coupled with the scanning electron microscopy, was used to detect phases.

The textural features were analyzed with FE-SEM using BSE. Images were collected at different magnifications to accurately characterize the textures and the distribution of phases (150X, 400X, 800X, and 1,500X). About 100 FE-SEM images were collected and used for the determination of phase content, abundance, and distribution by image analysis. Image analysis was performed using the Image-ProPlus 6.0 software by applying the same analytical protocol as reported in Iezzi et al. (2011) and Vetere et al. (2013, 2015). For each run product the identification of phases was determined by linking their gray-level ranges with the compositions.

## 4. Results

### 4.1. Liquidus Temperature and Composition of Residual Glasses

The liquidus temperature ( $T_L$ ) of the investigated composition was estimated using the alphaMELTS software package (Asimow et al., 2004; Smith & Asimow, 2005), providing a value for  $T_L = 1539$  K. Experimental data are in good agreement with this estimate since the experiment performed at  $T = 1530$  K did not show the presence of crystals, whereas experiments performed at 1516 K showed an increase in viscosity, confirming a possible rearrangement of the melt structure and/or nucleation and growth processes. The compositions of residual glasses of the crystal-bearing run products are reported in Table 1 in comparison with the starting material. The residual melt evolution resulted to be dependent on the applied shear rate, cooling temperature, and related run time. The faster the shear rate, the higher the SiO<sub>2</sub> content (please compare experiments TF0.1-2 and TF1-1) of the residual glass. The apparent anomaly for sample TF0.1-1 compared to TF0.1-2 is due to the longer duration (approximately 36,700 s) of the TF0.1 experiment as explained below.

### 4.2. Crystal Chemistry

Experiments at subliquidus condition were performed at a cooling rate of 10 K/hr from superliquidus temperature (1623 K) down to 1468 K. Two shear rates of 0.1 and 1 s<sup>-1</sup> were applied. BSE images were collected on samples cut perpendicular and parallel to the spindle axis (Figure 1d). Selected BSE images are shown in Figures 2 and 3. Figures 2a, 2b, 3a, and 3b report BSE images from the experiment performed at 0.1 s<sup>-1</sup>; Figures 2c, 2d, 3c, and 3d represent the quench product after viscosity measurement at 1 s<sup>-1</sup>. Both shear rate experiments were carried out under the previously defined cooling rate (10 K/hr).

Since samples were drilled out and recovered cylinders have a diameter of 6 mm and a length of ~10 mm, the total area investigated is approximately 340 mm<sup>2</sup> for each experiment.

At experimental conditions, clinopyroxene (hereafter Cpx) crystals are the dominant phase with only a minor amount of Fe-Ti oxide. Low fraction of olivine is also present only in experiments performed at low

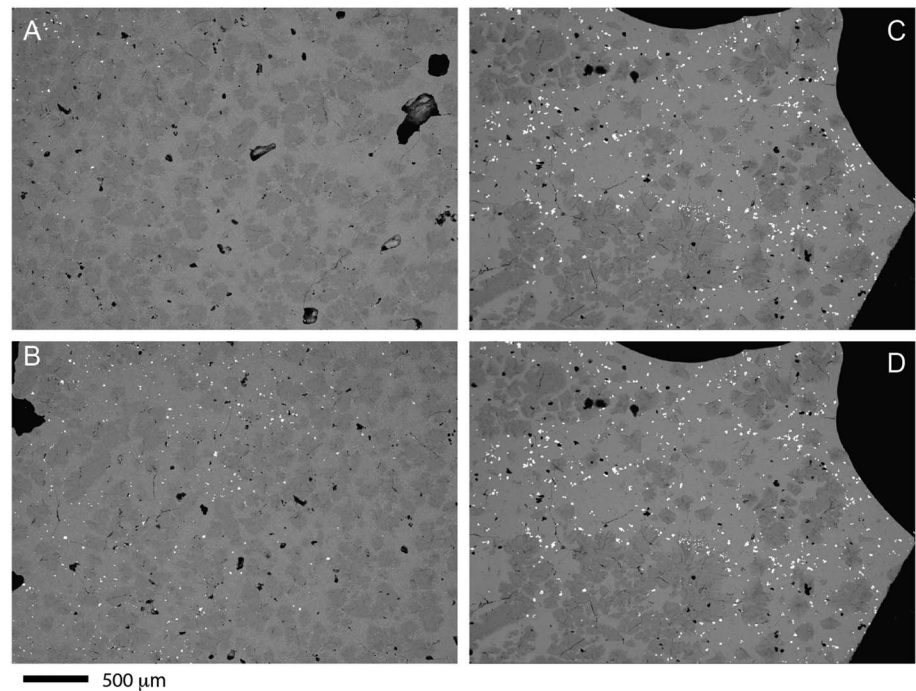


**Figure 2.** Selected backscattered electron images obtained after the experiments performed at shear rates of 0.1 and  $1 \text{ s}^{-1}$ . (a, b)  $\dot{\gamma} = 0.1 \text{ s}^{-1}$ . (c, d) Quench products after viscosity measurement at  $\dot{\gamma} = 1 \text{ s}^{-1}$ .

shear rate. The crystal fraction distribution as a whole shows no important deviations in volume between the experiments performed at different shear rates (i.e.,  $0.1$  and  $1 \text{ s}^{-1}$ ) and is calculated to be of approximately  $50.5 \pm 6.3$  and  $49.3 \pm 5.7$  vol %, respectively. Mass balance calculations give for the slow dynamic experiments (at shear rate =  $0.1 \text{ s}^{-1}$ )  $51.2$  vol % whereas for the  $1 \text{ s}^{-1}$  experiment  $53.1$  vol % of crystalline

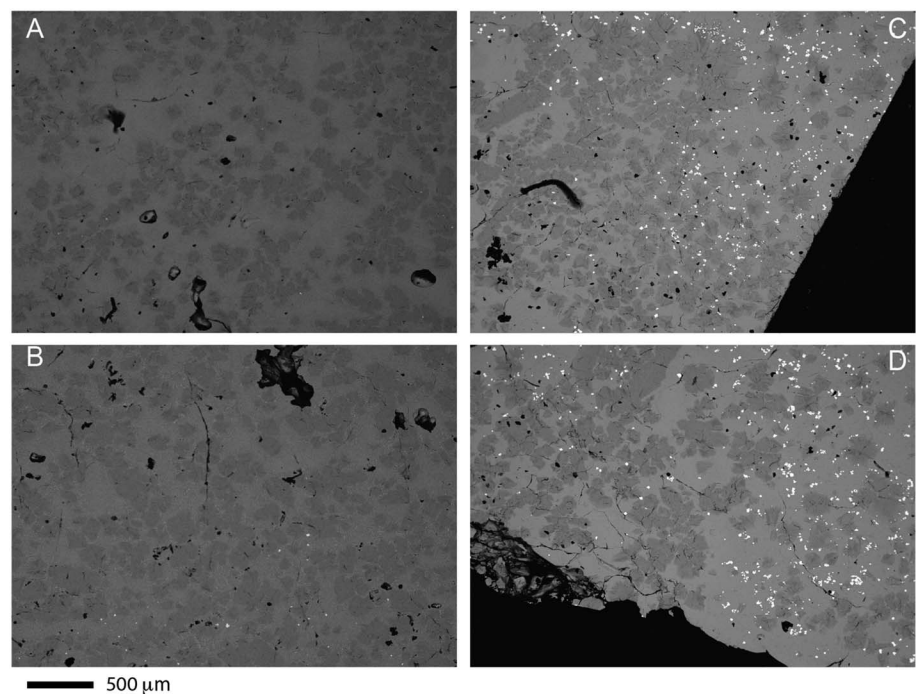


**Figure 3.** Additional backscattered electron details as in Figure 4 for shear rates of 0.1 and  $1 \text{ s}^{-1}$ . (a, b)  $\dot{\gamma} = 0.1 \text{ s}^{-1}$ . (c, d) Quench product after viscosity measurement at  $\dot{\gamma} = 1 \text{ s}^{-1}$ .

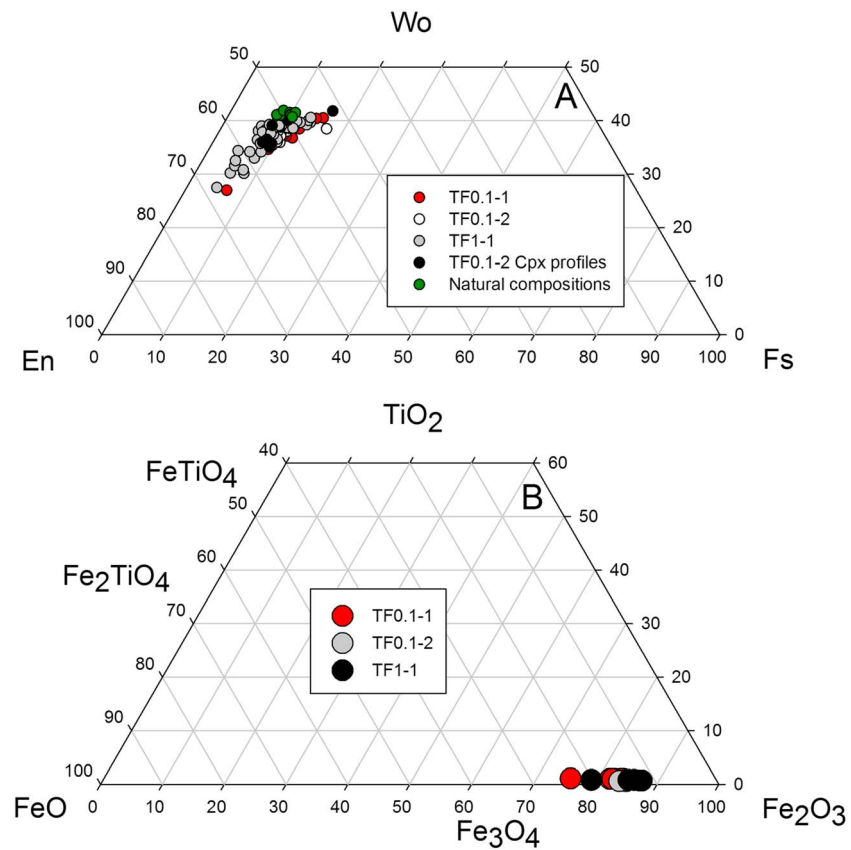


**Figure 4.** (a) Clinopyroxene (Cpx) and (b) Fe-Ti oxide crystal chemistry after experiments TF0.1-1, TF0.1-2, and TF1-1 (Table S3). Natural Cpx analyses are also reported for Cpx from the analyses by Lentz et al. (1999).

phases. Moreover, PhasePlot simulation (based on Ghiorso & Sack, 1995; Gualda et al., 2012; Ghiorso et al., 2002; Stixrude & Lithgow-Bertelloni, 2011) on Theo's Flow bulk compositions shows, at 1473 K, an amount of crystals of 48.6 vol %, very close to what has been measured above with a composition matching that obtained experimentally ( $Wo_{37}En_{51}Fs_{11}$ ; see below).

Both experiments exhibit similar amount of pyroxene, although there is a tendency to form more concentrated clusters in experiments performed at higher shear rates (Figures 3a–3c). Also, as shown in Figures 2c, 2d, 3c, and 3d, Fe-Ti oxides crystallize in all experiments (Figure 2 and 3) although they are quantified to be <2 area %. Pyroxenes frequently show complex clusters and a rounded habit and sometimes present slightly elongated shapes on the order of a few hundreds of micrometers. Also, some of them show complex growth history and clear chemical zonation corresponding, for the lighter part, to higher Fe and Ca contents, whereas the dark part is more enriched in Mg content (see below and Figure 4a).

Cpx compositional variation (from  $Wo_{27}En_{68}Fs_4$  to  $Wo_{42}En_{41}Fs_{17}$ ) shows a similar trend for all the three experiments, almost matching the natural Cpx composition from Theo's Flow (Lentz et al., 2011; Figure 4 a and Tables S1 and S2 in the supporting information). Moreover, at the beginning of the crystallization process, as recently highlighted by Mollo et al. (2018), melt compositional gradient produces Cpx growth layers as a response. This will produce a progressive enrichment in Al, Ti, and Na and depletion in  $Fe^{2+}$ , Ca, and Mg while increasing the degree of undercooling (Mollo et al., 2010, 2011, 2012). In particular, the surrounding melts will be depleted in Al and Fe and the feeding available ingredients will cause an overgrowth of Mg-rich Cpx. We are confident that what has been shown in Figures 5a and 5b corresponds exactly to the abovedescription as also demonstrated by EPMA data provided in Table S1 (core-to-rim CPx analyses).

Fe-Ti oxide crystals are much smaller (approximately 10  $\mu m$  or less) and in some cases more spherical. Composition is close to magnetite with slight chemical variation when considering all the three experiments (Figures 4b, 5a, and 5b and Tables S1 and S2). Furthermore, only in experiments performed at lower shear



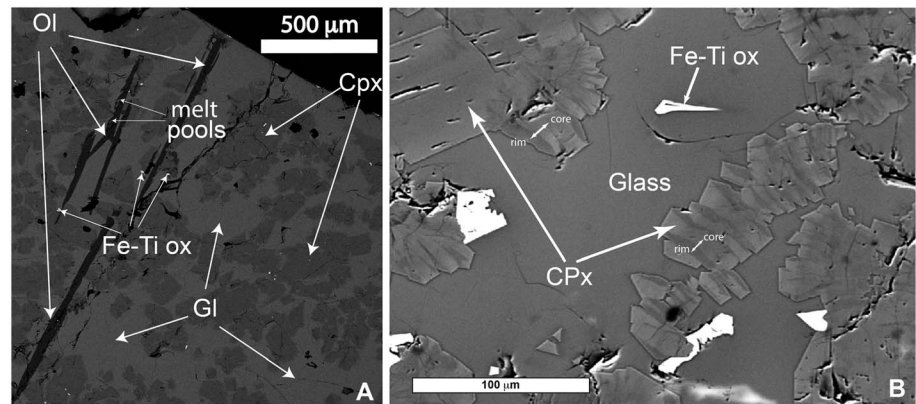


**Figure 5.** (a) Insight on the low-shear-rate experiment TF0.1-1 with high-aspect-ratio olivine (Ol), darker gray clinopyroxenes (Cpx), and light gray glass (Gl). Bright spots refer to iron and titanium oxides (Fe-Ti ox). (b) Texture features of the Cpx showing bright and dark areas possibly related to a second generation of Cpx (please refers to Table S1 for chemical composition details).

rate ( $\dot{\gamma} = 0.1 \text{ s}^{-1}$ ) were few olivine crystals found with a composition close to pure forsterite ( $\text{Fo}_{96-97}$ , Figure 5a). The reported data are the results of chemical analyses of about 130 crystals analyzed by means of electron microprobe (Tables S1 and S2).

### 4.3. Melt Viscosity

Melt viscosity was measured at different shear rates always equal to or higher than  $13 \text{ s}^{-1}$ . Such a relatively high shear rate was necessary due to the high fluidity of melt, as previously mentioned. Sixteen independent superliquidus experiments were performed in the temperature range between 1646 and 1530 K to determine the dependence of melt viscosity on temperature (Table 2 and Figure 6). In the investigated temperature range, viscosity varies from 2.2 to 7.8 Pa·s. Each viscosity value presented in Table 2 is an average between 100 and 500 readings, collected on timescales from 60 to 120 min, with torque values recorded every 5 to 30 s. The majority of the measurements were performed at a shear rate of  $13 \text{ s}^{-1}$ .

**Table 2**  
Viscosity Measurements as a Function of Temperature and Shear Rate

Experiment	$T$ (K)	$h$ (Pa·s)	std	Shear rate ( $\text{s}^{-1}$ )
TF-1	1646	2.2	0.35	13
TF-2	1618	2.9	0.23	13
TF-3	1586	4.3	0.03	13
TF-4	1583	4.1	0.02	13
TF-5	1578	4.8	0.03	13
TF-6	1569	5.3	0.03	13
TF-7	1558	5.9	0.06	13
TF-8	1545	6.5	0.03	13
TF-9	1545	6.6	0.02	13
TF-10	1543	6.2	0.1	13
TF-11	1535	7.3	0.03	13
TF-12	1530	7.8	0.05	13
TF-13	1545	6.4	0.02	20
TF-14	1543	6.5	0.1	20
TF-15	1535	7.2	0.03	15
TF-16	1530	7.7	0.05	15

*Note.* Experimental conditions and results of viscosity measurements ( $\eta$ ) using the concentric cylinder apparatus. Note that the value for each measurement is a single measurement on a pure-liquid system.  $\dot{\gamma}$  refers to the applied shear stress. No differences were found pointing to a Newtonian behavior of this system at the investigated shear rates; std refers to standard deviation of viscosity measurements.

To check for possible dependence of viscosity upon shear rate ( $\dot{\gamma}$ ), we repeated four experiments at 1545, 1543, 1535, and 1530 K with  $\dot{\gamma}$  ranging from 15 to  $20 \text{ s}^{-1}$  (samples TF-13 to TF-16 in Table 2). As it is evident in Figure 6 and Table 2, data are in very good agreement and no measurable effect of shear rate on viscosity was detected at superliquidus temperature.

An empirical model of viscosity as a function of temperature was developed by using the obtained viscosity data set. The model is based on the Vogel-Fulcher-Tammann (VFT) equation (Vogel, 1921), as follows:

$$\log \eta \text{ (Pa·s)} = A + B/(T - T_0) \quad (3)$$

where  $T$  is the temperature in kelvin, while  $A$ ,  $B$ , and  $T_0$  are fitting parameters, representing the preexponential term, the pseudo-activation energy (related to the barrier of potential energy obstructing the structural rearrangement of the liquid), and the VFT temperature, respectively. The VFT approach accounts for the non-Arrhenian temperature dependence of melt viscosity. Data were fitted using a nonlinear least squares regression providing the following parameters:  $A = -4.22$  (Pa·s),  $B = 4982.0$  (K), and  $T_0 = 556.1$  (K). This relationship reproduces our experimental data with a root mean square deviation of 0.016 (Figure 6). Note that the fitting parameters reported above are only valid for high-temperature (superliquidus) viscosity data.

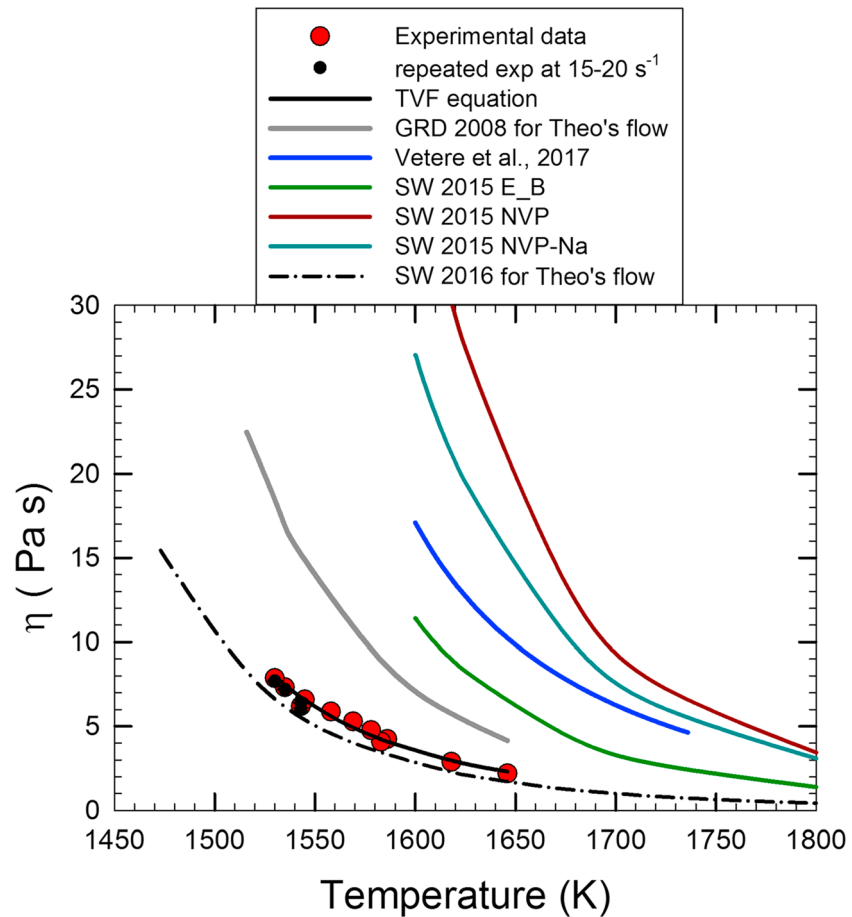


**Figure 6.** Viscosity data for melts at superliquidus conditions. The black line represents the predictive model given in equation (1). Red circles refer to experimental data performed at  $\dot{\gamma} = 13 \text{ s}^{-1}$ , while black circles refer to the repeated experiment performed at higher shear rates of 15 and  $20 \text{ s}^{-1}$ , suggesting a Newtonian behavior of such melts at the experimental high temperatures. The gray line refers to viscosity data derived from Giordano et al. (2008) by using our starting material composition. Colored lines, from top to bottom, refer to literature data of high fluid “mercurian” melts reported by Vetere et al. (2017) and Sehlke and Whittington (2015), respectively. The black dashed line (SW 2016) refers to the Sehlke and Whittington (2016) model for tholeiitic liquids.

An important feature of our composition is the relatively low  $\text{SiO}_2$  and the low  $\text{Al}_2\text{O}_3$  (5.65 wt %) contents. The high-MgO contents are responsible for the low viscosity of our silicate melt. Previous experimental data (e.g., Vetere et al., 2017) are in agreement with the lower melt viscosity described here. The comparison of the experimental viscosity data with those derived by the general model proposed by Giordano et al. (2008) shows a maximum difference of 10.0 Pa·s at 1530 K (Figure 6). Moreover, Sehlke and Whittington (2016) provided a model based on the Adam-Gibbs theory to relate viscosity ( $\eta$ ) to absolute temperature ( $T$ ) and the configurational entropy of the system ( $S_{\text{conf}}$ ). The modeled data are in excellent agreement with our experimental data for the composition of Theo’s Flow as shown in Figure 6. Finally, Liebske et al. (2005) and Dingwell et al. (2004) investigated the viscosity of peridotite melts from room pressure to approximately 13 GPa. Their results show low viscosities (approximately 0.1 Pa·s at 1850 K at 1 atm) that agree with the values obtained by using equation (3) (approximately 0.4 Pa·s at 1850 K).

#### 4.4. Partly Crystallized Rheology Under Cooling

Viscosity evolutions during cooling at shear rates of 0.1 and  $1 \text{ s}^{-1}$  are shown in Figures 7a and 7b. Viscosity trends show typical S-type curve evolution through time. Experiments were conducted for about 25,000 s applying identical cooling rates (10 K/hr). As shown in different literature studies (e.g., Mader et al., 2013, and reference therein), viscosity increase is primarily due to nucleation and crystal-growth processes

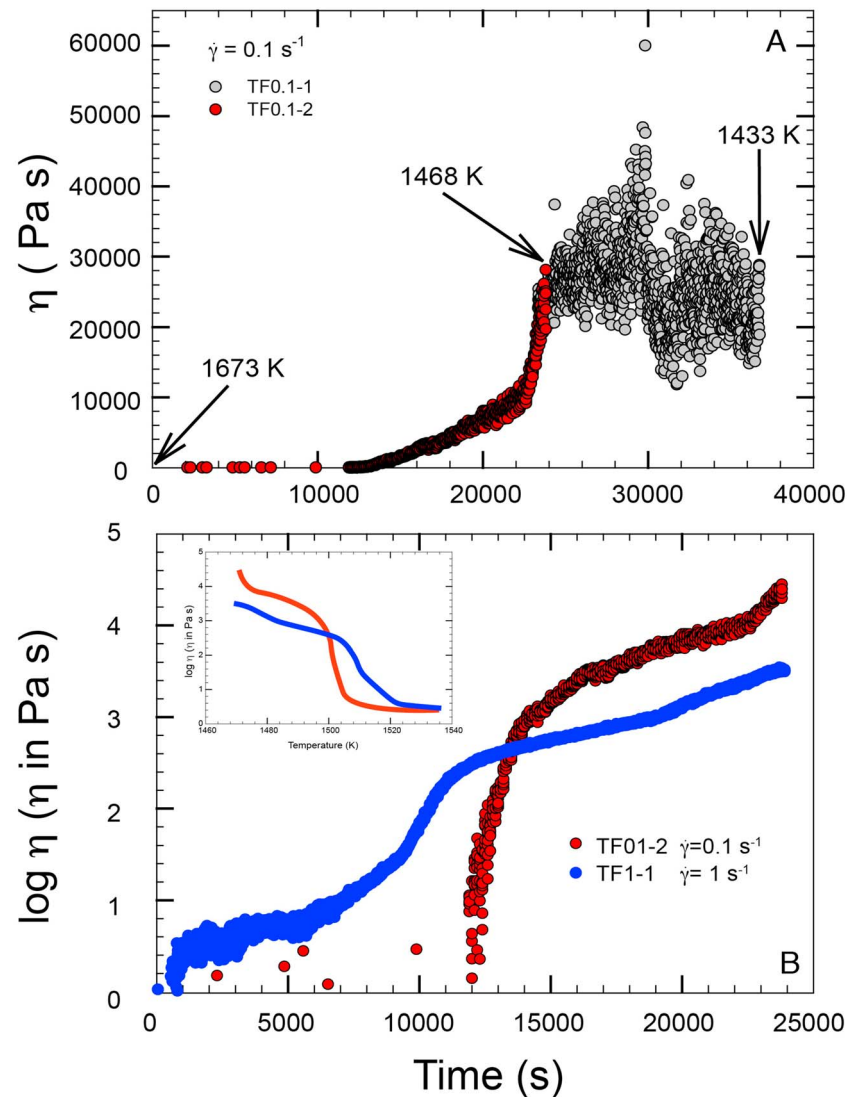


**Figure 7.** (a) Apparent viscosity versus time path at a rate of 10 K/hr for TF0.1-1 and TF0.1-2 experiments. Note the anomalous viscosity data reading for TF0.1-1 caused by a circular fracture of the melt + crystal system. The detachment points to a brittle failure of the system when viscosity reached the value of approximately 4.77 log (Pa·s) at 1468 K. In particular, the highest viscosity measured (approximately  $6.0 \times 10^4$  Pa·s) at a shear stress of 5960 Pa possibly corresponds to the brittle failure in this system (see text for further details). (b) Apparent viscosity versus time path and a related cooling rate of 10 K/hr. Note the continuum increase in viscosity and change in the viscosity versus time slopes as cooling proceeds. Difference of about 1 log units in effective viscosity points to evident shear thinning at the imposed shear rates. The symbol covers  $\pm 0.2$  log units of viscosity. The inset represents log viscosity versus temperature path for the TF0.1-2 and TF1-1 experiments.

under cooling, although the compositional evolution of the melts during crystallization needs to be considered. The experiment performed at  $0.1 \text{ s}^{-1}$  was repeated twice. The first experiment was run for a longer time (approximately 36,700 s; Figure 7a) and, after approximately 24,000 s we recorded anomalous and scattered viscosity values when temperature was below 1468 K (e.g., spikes in viscosity-versus-time plot; Figure 7a). After quenching ( $T = 1433 \text{ K}$ ), it was clear that the anomalous viscosity was caused by a circular fracture of the melt + crystal system located approximately at 0.7 cm from the spindle wall. A detachment between a part of the sample stacked on the spindle and all the rest of the sample into the crucible was clearly visible, pointing to a brittle failure of the system when viscosity reached the value of approximately 4.77 log (Pa·s) at 1468 K. In particular, the highest viscosity measured (approximately  $6.0 \times 10^4$  Pa·s) at a shear stress of 5960 Pa possibly corresponds to the brittle failure in our system. For such a

reason, to have a reasonable comparison between experiments, the subsequent runs were stopped soon after the temperature reached 1470 K. As expected, in both TF0.1-2 and TF1-1-1 experiments no brittle behavior was observed. Considering experiments performed at the lowest shear rate ( $0.1 \text{ s}^{-1}$ ), a sudden increase in viscosity after 12,000 s during continuous cooling was observed (Figure 7b). Viscosity data collected before 12,000 s are scattered and not useful since the relatively low applied shear rate does not allow the instrument to provide reliable data (i.e., the lower torque limit is reached due to the high fluidity/low viscosity); the experiments conducted at a higher shear rate show the beginning of the increase in viscosity much earlier, at around 5,000 s. The two viscosity curves cross each other after approximately 13,000 s (Figure 7b), where viscosity has a value of approximately 400 Pa·s and the temperature is close to 1500 K. Evolution of the viscosity curves, after 13,000 s, clearly points to a decrease in the apparent viscosity (i.e., the shear rate-versus-shear stress curve does not show linearity) as shear rate increases, with final viscosities of 4,000 and 32,000 Pa·s for TF1-1 and TF0.1-2, respectively (Figure 7b) also considering the fact that the amount of solid phases in TF0.1-2 and TF1-1 is almost identical at the quenching temperature (as shown above).

## 5. Discussion

### 5.1. Rheological Evolution

Our results show that the shear rate affects the composition of crystalline phases and the temperature at which they appear. In particular, the few olivine crystals that are present only in the experiment performed at low shear rate are almost pure forsterite in composition. These crystals exhibit large grain sizes ( $>1 \text{ mm}$ ) and typical habits due to a nonequilibrium crystallization (i.e., smoothed and with melt pools; see Figure 5a). These olivines represent the high-temperature phase starting their nucleation and growth soon after  $T_L$  is crossed. Thus, the growth rate of olivine, although based on a limited number of crystals, at a cooling rate of 10 K/hr results to be relatively large and on the order of approximately  $5.34 \times 10^{-8} \text{ m/s}$ . Cpx have similar chemical composition (Figure 4a) showing similar volume content in both experiments TF0.1-2 and TF1-1-1 (see section 4.2 and Figures 2 and 3), while in TF0.1-1 (the longest experiments) Cpx show relatively higher crystallinity as confirmed by image analysis ( $65.4 \pm 7.3 \text{ area } \%$ ) and mass balance calculation (62.6 vol %). This is due to the longer run time (up to approximately 36,700 s) that allows reaching a lower temperature (1433 K) before quenching.

The non-Newtonian behavior of suspensions whose viscosity decreases under shear strain (change in apparent viscosity) has been already observed in isothermal experiments (e.g., Ishibashi, 2009; Ryerson et al., 1988; Soldati et al., 2016; Vetere et al., 2017; Vona et al., 2011). Contrary to the classical isothermal viscosity experiments (Campagnola et al., 2016; Vetere et al., 2017; Vona et al., 2011; Vona & Romano, 2013), as expected, during cooling, viscosity never reached a steady value because no equilibrium conditions of the liquid + crystal suspensions were achieved. This is due to the progressive increase of crystallinity with time (Figure 7). In fact, before quenching, the low-shear-rate experiment ends up with a viscosity value of 24,800 Pa·s, following an almost constant increase of the time-viscosity curve, except in the last segment where it gets steeper. As for the high-shear-rate experiment, viscosity reaches the value of 3,150 Pa·s, again following essentially two trajectories, first less steep and then steeper. The kinks in the viscosity time path, for the TF1-1 and TF0.1-2 experiments (Figure 7b), possibly suggest important changes in crystallinity occurring after 19,000 and 22,500 s, respectively. Such a change in slopes could reflect a second generation of Cpx (see lighter/darker Cpx in Figure 5b) and/or crystal aggregation processes as shown by Campagnola et al. (2016).

The viscosity ratio between TF1-1 and TF0.1-2 is nearly 10 (3.6 and 4.5 in log units), whereas Cpx aspect ratios in both TF0.1-2 and TF1-1 experiments are quite similar, ranging in average between 1 and 3. However, careful examination of Figure 7 points out the following considerations:

- a) The apparent viscosity data set derived from TF0.1 experiments shows relatively low and scattered values until a temperature of 1505 K. During this time range (up to approximately 12,000 s), values are not reliable although a qualitative analysis indicates that the apparent viscosity remains relatively low for longer time compared to experiments performed at higher shear rate. The Theo's Flow system represented by the TF0.1 experiment needs to cool from a superliquidus temperature to 1505 K and for about 3.3 hr before viscosity values become measurable (Figure 7 and Table S3). Then, once the temperature of

1505 K is reached, the apparent viscosity requires only approximately 24 min to increase up to approximately 400 Pa·s, while temperature decrease is only 5 K.

- b) The TF1-1 viscosity data set shows an apparent viscosity increase, which occurs much earlier than for TF0.1. This is related to the fact, as stressed above, that at lower shear rates, measurements are not feasible due to the instrument's torque limit. Here the viscosity curve shows the classical S-shape curve (Vetere et al., 2017, and reference therein) that allows us to infer nucleation and crystal-growth rate (Vona et al., 2011; Vona & Romano, 2013). As an example, considering (1) an experimental time of 24,800 s (2) a cooling rate of 10 K/hr, (3) a typical Cpx crystal size of 200  $\mu\text{m}$  (as common experimental products, as shown in Figures 2 and 3), and (4) a temperature range from  $T_1$  (1525 K) to 1473 K, this will correspond to an average growth rate of approximately  $8.06 \times 10^{-7}$  cm/s, which is about 1 log unit lower than the olivine growth rate, as reported above.

Our experimental viscosity data under cooling confirm that higher shear rates result in earlier and more important crystallization compared to low shear rates as reported in Kolzenburg et al. (2017). It is now widely accepted that the more rapid change in rheological behavior at higher strain rates results from increased crystallization rates. Two possible mechanisms could be involved in dynamic crystallization process: (a) a continuous “fresh ingredient” on individual crystal's surface that could facilitate the crystal growth as shown, for example, in simulation for magmatic conditions (Petrelli et al., 2016); and (b) the increased stirring that could efficiently create crystal nuclei, as suggested in literature (Cashman et al., 1999; Emerson, 1926; Vona & Romano, 2013).

Finally, the mentioned  $T_{\text{cutoff}}$  (or the temperature at which the system reaches its rheological death) and relative modeling were successfully tested for basaltic systems by Kolzenburg et al. (2019). Applying our cooling rate, it provides a value of approximately 1510 K where viscosity for TF1-1 and TF0.1-2 will be on the order of  $10^2$  Pa·s (far off from a possible rheological death of Theo's lava flow). This relatively low viscosity value possibly reflects the very different chemistry of our samples and those of Kolzenburg et al. (2019), preventing to derive a general model.

## 5.2. Possible Implications for Terrestrial and Martian Lava Flows

Literature data point to a wide range of possible compositions for magma that erupted on Mars with relatively low viscosity (e.g., augite basalt, NWA 8159 meteorite belonging to the Nakhilite suite or Shergottite with similar composition to the Bounce Rock interior; Sehlke & Whittington, 2016). Moreover, Udry and Day (2018) allow us to compare the bulk rock analyses of nakhilites and chassignites Martian meteorite with our starting composition. Considering that our experiments were performed at relatively oxidized condition and that ferrous iron in the natural composition can be substituted by Ca and Mg and ferric iron can be replaced by Al (Vetere et al., 2006, and reference therein), we are confident that our starting material can be considered as a possible Martian composition.

In terms of lava flowing ability, it is clear, from the experimental data, that magma and lava flow velocities are highly influenced by the dynamics to which the system is subjected. As we concentrated our study on the pyroxenite unit, we can use experimental viscosity data to investigate the magma velocities and relative possible emplacement mechanisms.

Theo's Flow is chemically similar to the composition of nakhilites, a suite of medium-grained pyroxenite meteorites that may have been erupted as lava flows on Mars and may therefore be a suitable proxy for such lavas. Martian surface gravity is about  $3.71 \text{ m/s}^2$  (i.e., about 38% that of the Earth) and shows also variations with latitude. This fact will reduce the lava flow speed on Mars surface. As previously reported, at any given scale, processes such as fluid convection and consequent convective heat transfer, crystal settling due to positive or negative buoyancy will be slower on Mars compared to that on Earth due to lower gravity. For identical reason, magma ascent rates on Mars will be slower compared to those on Earth (Wilson & Head, 1994).

It has been demonstrated recently that very wide and extended lava flows on Mars possibly occurred during its volcanic history due to high effusion rates (Hopper & Leverington, 2014; Leverington, 2018). In such a context, the rheology of Martian magma has been poorly quantified essentially because magma compositions are difficult to be constrained from Martian flow morphologies (Bandfield et al., 2000; Mouginitis-Mark et al., 1984). Considering the pyroxenite of Theo's Flow as one of the possible compositions erupted on Mars and considering that (1) Fe-rich lunar mare basalt seems to exhibit only a small increase in

crystal fraction over the first ~125 K of cooling (Morrison et al., 2019), allowing an extended period of flow at a relatively low viscosity and that (2) very low viscosities are necessary to build very wide and long magma flow units (Hopper & Leverington, 2014; Leverington, 2018), we can infer relatively high eruption temperature. Following this hypothesis and inferring a relatively high ascent rate (although Martian gravity may reduce the ascent velocity), we measured a viscosity of approximately 2 and 8 Pa·s in a temperature range of 1646–1530 K, respectively. Using the experimental viscosity data to infer velocity evolution considering terrain slopes values between 0.1° and 10° and lava flow thicknesses from 1 to 10 m, a magma velocity can be calculated using the approach proposed by Williams et al. (2001), assuming a turbulent lava flow due to its very high fluidity. Lava flow velocity  $u$  (m/s), is calculated considering (1) the ground slope ( $\theta$ ) and (2) the lava friction coefficient  $\lambda$  that is related to the Reynolds number (Re).  $\lambda$  is defined as the ratio between the shear stress at the solid surface and the kinetic energy of the fluid elements. The friction coefficient, being dimensionless, depends on the velocity ( $u$ ), the thickness of the conduit or channel, the density ( $\rho$ ), and the viscosity ( $\eta$ ). The surface roughness also has to be taken into account. These quantities can be rearranged as  $\rho u h / \eta$ , which is the Re. In case of a laminar flow, a simple mathematical treatment gives  $f = 16/\text{Re}$  for  $\text{Re} < 2,000$ . More complex is the case for turbulent flows, for which the roughness of a hypothetical conduit must also be considered. The solution proposed here is given by Kakaç et al. (1987) and used in Williams et al. (2001) and also in Byrne et al. (2013).

The following equations (4)–(6) (Williams et al., 2001) are valid only in the case of high  $\text{Re} \gg 2000$ :

$$u = \sqrt{\frac{4gh \sin(\theta)}{\lambda}} \quad (4)$$

where  $g$  ( $\text{m/s}^2$ ) is the acceleration due to gravity and  $h$  (m) the lava flow thickness.  $\lambda$  can be calculated as follows:

$$\lambda = \frac{1}{[0.79 \ln(\text{Re}) - 1.64]^2} \quad (5)$$

where Re is the Reynolds numbers defined as

$$\text{Re} = \frac{2\rho u h}{\eta} \quad (6)$$

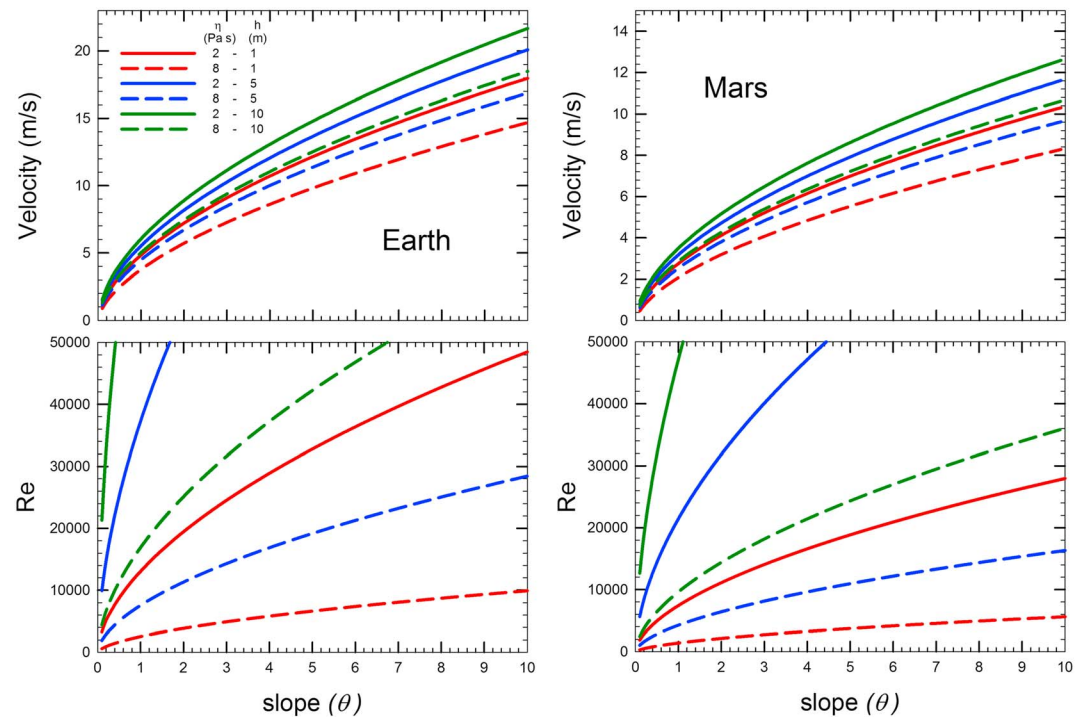
where  $\rho$  is the bulk lava density ( $2,698 \text{ kg/m}^3$ ) for the melt considered here, as calculated in Table 1, and  $\eta$  is the lava viscosity (Pa·s).

Figure 8 shows velocities versus slope (°) calculated after solving iteratively equations (4)–(6) by changing the lava flow thickness from 1 to 10 m and viscosity from 2 to 8 Pa·s for both Earth and Mars environments (Table S4). Results provide relatively high velocities ranging from 0.9–14.7 and 0.5 to 8.3 m/s for lava flows on Earth and Mars even if gravity on Mars is almost one third that of Earth (e.g., 9.81 and 3.71  $\text{m/s}^2$ , respectively; calculation is based on 1-m-thick lava having a viscosity of 8 Pa·s flowing on slopes from 0.1° to 10°). These assumptions are valid only when considering a geological scenario in which magma eruption temperature is above  $T_L$ , although possible delay in crystallization could happen (e.g., if the dynamics of the system slow down as shown in Kolzenburg et al., 2019), allowing a long-lasting low viscosity.

If eruption temperature is lower than  $T_L$ , processes such crystal nucleation and growth will take place and drastically affect viscosity. The evolution of viscosity and velocity during cooling is thus related to the amount of crystalline phases and their evolution during cooling, as for the experiments presented here. Although we are aware that a direct control on the evolution of solid phases during cooling is not accessible in our experiments, we do have a direct control on the viscosity-time progress so that we can track velocity change during cooling. In fact, as a first approximation, we can adopt Jeffrey's equation as proposed also in Parfitt and Wilson (2008), keeping in mind that the following equation is applicable to Newtonian fluids:

$$u = \frac{d^2 \cdot \rho \cdot g}{3 \cdot \eta} \cdot \sin \theta \quad (7)$$

where  $u$  (m/s) is velocity,  $d$  (m) is the channel depth,  $g$  ( $\text{m/s}^2$ ) is the acceleration due to gravity, and  $h$  (m) is the lava flow thickness, and  $\rho$  is the bulk lava density. From equation (7), it is evident that the steeper the



**Figure 8.** Velocity profiles for terrestrial and Martian environments and relative Reynolds number calculated from equations (4)–(6) by using the experimental viscosity data ( $\eta$ ) and a lava flow at 1, 5, and 10 m in depth (hr).

slope or the lower the viscosity, the higher the velocity. Also, it must be pointed out that viscosity data represent the evolution of the ability to flow under a defined cooling rate of 10 K/hr. Following observations by Vetere et al. (2015), we can possibly assess that this cooling rate applies at approximately 20-cm depth (note, however, that experiments by Vetere et al., 2015, were conducted at static conditions with different cooling rates and different compositions along a basaltic to rhyolitic join).

In order to track the velocity evolution of a cooling lava flow with different slopes and flow depths, we used data presented in Figure 8. Calculated velocities for Mars and Earth (Figures S1 and S2 and Table S4 in the supporting information) environments are provided according to equation (7). As an example, considering a lava flow depth of 5 m, and three different slopes ( $0.1^\circ$ ,  $1^\circ$ , and  $10^\circ$ ), lava flows with a higher shear rate (Figure S2, TF1-1 Mars; and Figure S3, TF1-1 Earth) on very gentle slopes have still the power to continue (although at a relatively low velocity, approximately 0.05 m/s) to flow, while lava flows having a lower shear rate (Figure S2, TF0.1-2 Mars; and Figure S3, TF0.1-2 Earth) will be subjected to a drop in velocity (below  $0.01 \text{ m}\cdot\text{s}^{-1}$ ) much earlier. On the other hand, final velocities related to our highest measured viscosities, considering a terrain slope of  $1^\circ$ , vary between 0.05 (Mars) and 0.1 m/s (Earth) if the shear rate is  $0.1 \text{ s}^{-1}$ , while velocity values increase to approximately 0.4 (Mars) and 1 m/s (Earth) when the shear rate is  $1 \text{ s}^{-1}$ .

Identical calculations are provided for different terrain slopes and lava flow depths for slopes of  $0.1^\circ$ ,  $1^\circ$ , and  $10^\circ$  and for 1, 5, and 10 m of thicknesses, confirming that shear stress plays an important role on velocities, allowing hypothetical lava to flow at a relatively high speed in case of a higher applied shear rate (Figure S2 and S3).

Finally, by considering the eruption temperature close to the liquidus temperature (1525 K), we can estimate the maximum flow length versus time by using our experimental viscosity data provided in Figure 7 and equation (1). Wilson et al. (2009) provided (other than equation (7) for laminar flow) a solution in case of turbulent flow occurrence, thus for Re exceeding the value of 2,000. In this case, the velocity of lava flowing in a turbulent regime ( $u_t$ ) can be related, as in equation (5), to the flow depth,  $d$ ; the acceleration due to gravity,  $g$ ; the terrain slope of the preexisting topography,  $\theta$ ; and the friction factor  $f$ , as follows:

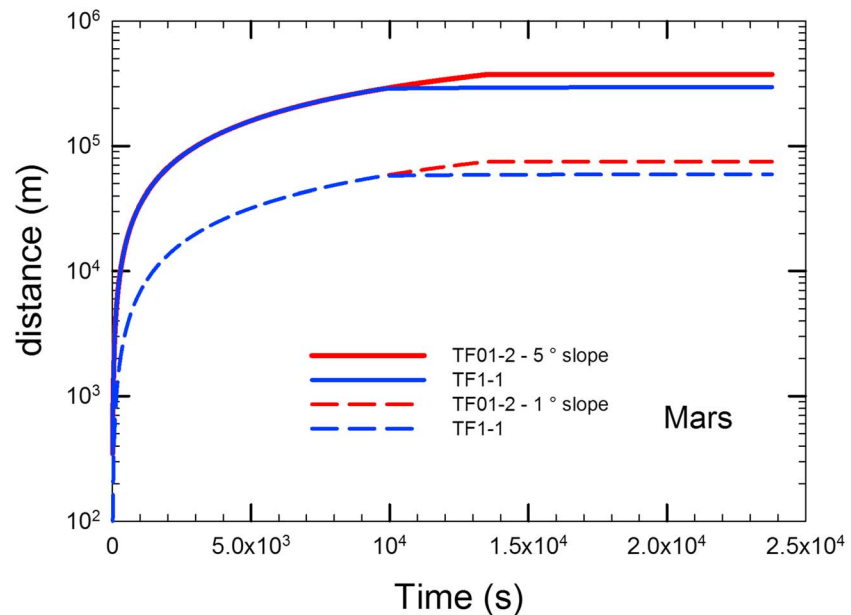


**Figure 9.** Distance versus time profiles for the Martian environments calculated from equations (8) and (9) by using the experimental viscosity data ( $\eta$ ) as in Figure 7 and Tables 3 and S3.

$$u_t = [(2gd \sin \theta)/f]^{1/2} \quad (8)$$

where  $f$ , in fully turbulent flow, is

$$f = 0.32 / \text{Re}^{0.25} \quad (9)$$

Our viscosity data and related Re calculations (Table S5) suggest turbulent flows for terrain slopes close to or greater than  $1^\circ$ . Results are provided in Figure 9 for terrain slopes of  $1^\circ$  and  $5^\circ$ . Although these calculations are made on the unlikely assumption of constant slopes, we can, at least, have an idea about the possible travel distance for very fluid magmas. As an example, with  $1^\circ$  terrain slope and  $d$  equal to 1 m, on Mars, lavas are able to flow approximately for 375 and 296 km if viscosity data obtained at shear rates of  $0.1$  and  $1 \text{ s}^{-1}$  are used, respectively. Identical consideration gives magma travel distances of approximately 75 and 60 km if the terrain slope is  $5^\circ$ . It should be noted that the time required for these travel distances are only approximately 7 hr. Figure 9 proves that in order to travel very long distances, Martian magmas must have very high eruption temperatures and low viscosity, implying very low crystal cargo.

## 6. Conclusions

New viscosity experiments performed at superliquidus and during cooling of  $10 \text{ K/hr}$  have been performed at different shear rates on a pyroxenite composition derived from the Theo's Flow. Results revealed that this composition is extremely fluid at temperatures between  $1643$  and  $1530 \text{ K}$ , and measured viscosities are between  $2.2$  and  $7.8 \text{ Pa}\cdot\text{s}$ . Such very low viscosities allow the lava to flow in a turbulent regime as confirmed by the high Re numbers, which are usually  $>2,000$  for likely values of lava flow thickness and ground slope. As a consequence, very long distances (up to  $375 \text{ km}$ ) could be covered by the lava flows if the effusion rate is high, preventing dramatic heat loss due to turbulence (Vetere et al., 2017). If we assume that the studied composition is a good proxy for Mars lava flows and with very high effusion rates, our results might explain the presence of extraordinary large volcanic channels, as recently hypothesized for the Kasei Valles on Mars, even considering that the gravity is approximately one third that of Earth (Leverington, 2018). Few literature data tracking viscosity during cooling are available, most of which are performed at isothermal conditions, and they reported shear thinning effect on different compositions (e.g., Ishibashi, 2009; Kolzenburg et al., 2016, 2017; Kolzenburg, Giordano, et al., 2018; Ryerson et al., 1988; Vetere et al., 2017; Vona et al., 2011). Our experiments have shown an apparent viscosity change behavior during cooling as a result of the



applied shear rates ( $0.1$  and  $1 \text{ s}^{-1}$ ), confirming that the rheology of lava flows needs to be studied under dynamic (i.e., nonequilibrium) conditions to better understand the real geological scenarios occurring in magmatic and volcanic systems.

### Acknowledgments

This research was funded by the European Research Council Consolidator Grant ERC-2013-COG No. 612776 (CHRONOS project) to D. Perugini and by the F.R.B. TESLA to F. Vetere. Alexander von Humboldt Foundation Senior Research Grant to F. Vetere is also acknowledged. M. A. and M. M. are supported by the European Research Council (ERC) under the European Union's Horizon 2020 Research and Innovation Programme (grant agreement 714936 for the project TRUE DEPTHS to M. Alvaro). M. C. D. has been supported by the PNRA 2016 Antarctic Meteorites to Luigi Folco. Data of experiments are reported in Tables 1 and 2, in Figures 1–9, and in the supporting information as Tables S1–S5 and Figures S1–S3.

### References

- Alvaro, M., Domeneghetti, M. C., Fioretti, A. M., Cámara, F., & Marinangeli, L. (2015). A new calibration to determine the closure temperatures of Fe-Mg ordering in augite from nakhlites. *Meteoritics & Planetary Science*, *50*(3), 499–507. <https://doi.org/10.1111/maps.12436>
- Angell, C. A. (1985). Strong and fragile liquids. In K. Ngai, & G. Wright (Eds.), *Relaxation in complex systems*, (pp. 3–11). Virginia: National Technical Information Service, U.S. Department of Commerce, Springfield.
- Arndt, N. T. (1977). Thick, layered peridotite–gabbro lava flows in Munro Township, Ontario. *Canadian Journal of Earth Sciences*, *14*(11), 2620–2637. <https://doi.org/10.1139/e77-227>
- Arzilli, F., & Carroll, M. R. (2013). Crystallization kinetics of alkali feldspars in cooling and decompression-induced crystallization experiments in trachytic melt. *Contributions to Mineralogy and Petrology*, *166*(4), 1011–1027. <https://doi.org/10.1007/s00410-013-0906-1>
- Asimow, P. D., Dixon, J. E., & Langmuir, C. H. (2004). A hydrous melting and fractionation model for mid-ocean ridge basalts: Application to the mid-Atlantic ridge near the Azores. *Geochemistry, Geophysics, Geosystems*, *5*, Q01E16. <https://doi.org/10.1029/2003GC000568>
- Bandfield, J. L., Hamilton, V. E., & Christensen, P. R. (2000). A Global view of Martian surface compositions from MGS-TES. *Science*, *287*(5458), 1626–1630. <https://doi.org/10.1126/science.287.5458.1626>
- Byrne, P. K., Holohan, E. P., Kervyn, M., van Wyk de Vries, B., Troll, V. R., & Murray, J. B. (2013). A sagging-spreading continuum of large volcano structure. *Geology*, *41*(3), 339–342. <https://doi.org/10.1130/G33990.1>
- Campagnola, S., Vona, A., Romano, C., & Giordano, G. (2016). Crystallization kinetics and rheology of leucite-bearing tephriphonolite magmas from the Colli Albani volcano (Italy). *Chemical Geology*, *424*, 12–29. <https://doi.org/10.1016/j.chemgeo.2016.01.012>
- Caricchi, L., Burlini, L., Ulmer, P., Gerya, T., Vassalli, M., & Papale, P. (2007). Non-Newtonian rheology of crystal-bearing magmas and implications for magma ascent dynamics. *Earth and Planetary Science Letters*, *264*(3–4), 402–419. <https://doi.org/10.1016/j.epsl.2007.09.032>
- Carmichael, R. S. (1974). *Igneous petrology*, (p. 793). New York: McGraw-Hill.
- Cashman, K. V. (1993). Relationship between plagioclase crystallization and cooling rate in basaltic melts. *Contributions to Mineralogy and Petrology*, *113*(1), 126–142. <https://doi.org/10.1007/BF00320836>
- Cashman, K. V., Thornber, C., & Kauahikaua, J. P. (1999). Cooling and crystallization of lava in open channels, and the transition of pāhoehoe lava to 'a'ā. *Bulletin of Volcanology*, *61*(5), 306–323. <https://doi.org/10.1007/s004450050299>
- Chevrel, M. O., Baratoux, D., Hess, K.-U., & Dingwell, D. B. (2014). Viscous flow behavior of tholeiitic and alkaline Fe-rich Martian basalts. *Geochimica et Cosmochimica Acta*, *124*, 348–365. <https://doi.org/10.1016/j.gca.2013.08.026>
- Chevrel, M. O., Giordano, D., Potuzak, M., Courtial, P., & Dingwell, D. B. (2013). Physical properties of  $\text{CaAl}_2\text{Si}_2\text{O}_8$ - $\text{CaMgSi}_2\text{O}_6$ - $\text{FeO}$ - $\text{Fe}_2\text{O}_3$  melts: Analogues for extra-terrestrial basalt. *Chemical Geology*, *346*, 93–105. <https://doi.org/10.1016/j.chemgeo.2012.09.004>
- Chevrel, M. O., Harris, A. J. L., James, M. R., Calabrò, L., Gurioli, L., & Pinkerton, H. (2018). The viscosity of pāhoehoe lava: In situ syn-eruptive measurements from Kilauea, Hawaii. *Earth and Planetary Science Letters*, *493*, 161–171. <https://doi.org/10.1016/j.epsl.2018.04.028>
- Chevrel, M. O., Platz, T. b., Hauber, E. c., Baratoux, D., Lavallée, Y., & Dingwell, D. B. (2013). Lava flow rheology: A comparison of morphological and petrological methods. *Earth and Planetary Science Letters*, *384*, 109–120. <https://doi.org/10.1016/j.epsl.2013.09.022>
- Coffin, M. F., & Eldholm, O. (1994). Large igneous provinces: Crustal structure, dimensions, and external consequences. *Reviews of Geophysics*, *32*(1), 1–36. <https://doi.org/10.1029/93RG02508>
- Condie, K. C. (1981). *Archean greenstone belts*. Elsevier.
- Dingwell, D. B., Courtial, P., Giordano, D., & Nichols, A. R. L. (2004). Viscosity of peridotite liquid. *Earth and Planetary Science Letters*, *226*(1–2), 127–138. <https://doi.org/10.1016/j.epsl.2004.07.017>
- Dundas, C. M., & Keszthelyi, L. P. (2014). Emplacement and erosive effects of lava in south Kasei Valles, Mars. *Journal of Volcanology and Geothermal Research*, *282*, 92–102. <https://doi.org/10.1016/j.jvolgeores.2014.06.005>
- Emerson, O. H. (1926). The formation of aa and pāhoehoe. *American Journal of Science*, *s5-12*(68), 109–114. <https://doi.org/10.2475/ajs.s5-12.68.109>
- Fiege, A., Vetere, F., Iezzi, G., Simon, A., & Holtz, F. (2015). The roles of decompression rate and volatiles ( $\text{H}_2\text{O} + \text{Cl} \pm \text{CO}_2 \pm \text{S}$ ) on crystallization in (trachy-) basaltic magma. *Chemical Geology*, *411*, 310–322. <https://doi.org/10.1016/j.chemgeo.2015.07.016>
- Friedman, R. C., (1998). Petrologic clues to lava flow emplacement and post-emplacement processes [Ph.D. dissertation]: Honolulu, University of Hawaii at Manoa, 260 p.
- Ghiorso, M. S., Hirschmann, M. M., Reiners, P. W., & Kress, V. C. III (2002). The pMELTS: A revision of MELTS for improved calculation of phase relations and major element partitioning related to partial melting of the mantle to 3 GPa. *Geochemistry, Geophysics, Geosystems*, *3*(5), 1030. <https://doi.org/10.1029/2001GC000217>
- Ghiorso, M. S., & Sack, R. O. (1995). Chemical mass transfer in magmatic processes IV. A revised and internally consistent thermodynamic model for the interpolation and extrapolation of liquid-solid equilibria in magmatic systems at elevated temperatures and pressures. *Contributions to Mineralogy and Petrology*, *119*(2–3), 197–212. <https://doi.org/10.1007/BF00307281>
- Giordano, D. (2019). *Advances in the rheology of natural multiphase silicate melts: Import for magma transport and lava flow emplacement*. *Annals of Geophysics*, *61*. <https://doi.org/10.4401/ag-7859>
- Giordano, D., Polacci, M., Longo, A., Papale, P., Dingwell, D. B., Boschi, E., & Kasereka, M. (2007). Thermo-rheological magma control on the impact of highly fluid lava flows at Mt Nyiragongo. *Geophysical Research Letters*, *34*, L06301. <https://doi.org/10.1029/2006GL028459>
- Giordano, D., Russell, J. K., & Dingwell, D. B. (2008). Viscosity of magmatic liquids: a model. *Earth and Planetary Science Letters*, *271*(1–4), 123–134. <https://doi.org/10.1016/j.epsl.2008.03.038>
- Gualda, G. A. R., Ghiorso, M. S., Lemons, R. V., & Carley, T. L. (2012). Rhyolite-MELTS: A modified calibration of MELTS optimized for silica-rich, fluid-bearing magmatic systems. *Journal of Petrology*, *53*(5), 875–890. <https://doi.org/10.1093/ptrology/egr080>
- Hammer, J. E. (2008). Experimental studies of the kinetics and energetics of magma crystallization. *Reviews in Mineralogy and Geochemistry*, *69*(1), 9–59. <https://doi.org/10.2138/rmg.2008.69.2>

- Hiesinger, H., Head, J. W., & Neukum, G. (2007). Young lava flows on the eastern flank of Ascraeus Mons: Rheological properties derived from High Resolution Stereo Camera (HRSC) images and Mars Orbiter Laser Altimeter (MOLA) data. *Journal of Geophysical Research*, *112*, E05011. <https://doi.org/10.1029/2006JE002717>
- Hopper, J. P., & Leverington, D. W. (2014). Formation of Hrad Vallis (Mars) by low viscosity lava flows. *Geomorphology*, *207*, 96–113. <https://doi.org/10.1016/j.geomorph.2013.10.029>
- Hulme, G. (1974). The interpretation of lava flow morphology. *Geophysical Journal International*, *39*(2), 361–383. <https://doi.org/10.1111/j.1365-246X.1974.tb05460.x>
- Iezzi, G., Mollo, S., Torresi, G., Ventura, G., Cavallo, A., & Scarlato, P. (2011). Experimental solidification of an andesitic melt by cooling. *Chemical Geology*, *283*(3-4), 261–273. <https://doi.org/10.1016/j.chemgeo.2011.01.024>
- Ishibashi, H. (2009). Non-Newtonian behavior of plagioclase-bearing basaltic magma: Subliquidus viscosity measurement of the 1707 basalt of Fuji volcano, Japan. *Journal of Volcanology and Geothermal Research*, *181*(1-2), 78–88. <https://doi.org/10.1016/j.jvolgeores.2009.01.004>
- Ishibashi, H., & Sato, H. (2007). Viscosity measurements of subliquidus magmas: Alkali olivine basalt from the Higashi-Matsuura district, Southwest Japan. *Journal of Volcanology and Geothermal Research*, *160*(3-4), 223–238. <https://doi.org/10.1016/j.jvolgeores.2006.10.001>
- Jeffreys, H. (1925). The flow of water in an inclined channel of rectangular section. *The London, Edinburgh, and Dublin Philosophical Magazine and Journal of Science*, *6*(293), 793–807.
- Kakaç, S., Shah, R. K., & Aung, W. (1987). *Handbook of single-phase convective heat transfer*, (p. 900). New York, NY (USA): John Wiley and Sons Inc.
- Klöß, G.H., (2000). Dichtefluktuationen natürlicher Gläser (Dissertation) University of Jena.
- Kolzenburg, S., Di Genova, D., Giordano, D., Hess, K. U., & Dingwell, D. B. (2018). The effect of oxygen fugacity on the rheological evolution of crystallizing basaltic melts. *Earth and Planetary Science Letters*, *487*, 21–32. <https://doi.org/10.1016/j.epsl.2018.01.023>
- Kolzenburg, S., Giordano, D., Cimarelli, C., & Dingwell, D. B. (2016). In situ thermal characterization of cooling/crystallizing lavas during rheology measurements and implications for lava flow emplacement. *Geochimica et Cosmochimica Acta*, *195*, 244–258. <https://doi.org/10.1016/j.gca.2016.09.022>
- Kolzenburg, S., Giordano, D., Hess, K. U., & Dingwell, D. B. (2018). Shear rate-dependent disequilibrium rheology and dynamics of basalt solidification. *Geophysical Research Letters*, *45*, 6466–6475. <https://doi.org/10.1029/2018GL077799>
- Kolzenburg, S., Giordano, D., di Muro, A., & Dingwell, D. B. (2019). Equilibrium viscosity and disequilibrium rheology of a high magnesium basalt from Piton de la Fournaise volcano, La Reunion, Indian Ocean, France. *Annals of Geophysics*, *61*(Vol 61 (2018)), 18. <https://doi.org/10.4401/ag-7839>
- Kolzenburg, S., Giordano, D., Thordarson, T., Höskuldsson, A., & Dingwell, D. B. (2017). The rheological evolution of the 2014/2015 eruption at Holuhraun, central Iceland. *Bulletin of Volcanology*, *79*(6), 45. <https://doi.org/10.1007/s00445-017-1128-6>
- Krieger, I. M., & Elrod, H. (1953). Direct determination of flow curves of non-Newtonian fluid. II. Shearing rate in the concentric cylinder viscometer. *Journal of Applied Physics*, *24*(2), 134–136. <https://doi.org/10.1063/1.1721226>
- Lange, R. A., Cashman, K. V., & Navrotsky, A. (1994). Direct measurements of latent heat during crystallization and melting of a ugardite and an olivine basalt. *Contributions to Mineralogy and Petrology*, *118*(2), 169–181. <https://doi.org/10.1007/BF01052867>
- Lentz, R. C. F., McCoy, T. J., Collins, L. E., Corrigan, C. M., Benedix, G. K., Taylor, G. J., & Harvey, R. P. (2011). Theo's Flow, Ontario, Canada: A terrestrial analog for the Martian nakhlite meteorites. *The Geological Society of America Special Papers*, *483*, 263–277. [https://doi.org/10.1130/2011.2483\(17\)](https://doi.org/10.1130/2011.2483(17))
- Lentz, R. C. F., Taylor, G. J., & Treiman, A. H. (1999). Formation of a Martian pyroxenite: A comparative study of the nakhlite meteorite and Theo's Flow. *Meteoritics & Planetary Sciences*, *34*(6), 919–932. <https://doi.org/10.1111/j.1945-5100.1999.tb01410.x>
- Leverington, D. W. (2018). Is Kasei Valles (Mars) the largest volcanic channel in the solar system? *Icarus*, *301*, 37–57. <https://doi.org/10.1016/j.icarus.2017.10.007>
- Liebske, C., Schmickler, B., Terasaki, H., Poe, B. T., Suzuki, A., Funakoshi, K. I., et al. (2005). Viscosity of peridotite liquid up to 13 GPa: Implications for magma ocean viscosities. *Earth and Planetary Science Letters*, *240*(3-4), 589–604. <https://doi.org/10.1016/j.epsl.2005.10.004>
- Lofgren, G. (1980). Experimental studies on the dynamic crystallization of silicate melts. In R. B. Hargraves (Ed.), *Physics of magmatic processes*, (pp. 487–551). Princeton, NJ: Princeton University.
- Mader, H. M., Llewellyn, E. W., & Mueller, S. P. (2013). The rheology of two-phase magmas: A review and analysis. *Journal of Volcanology and Geothermal Research*, *257*, 135–158. <https://doi.org/10.1016/j.jvolgeores.2013.02.014>
- Mollo, S., Blundy, J., Scarlato, P., De Cristofaro, S. P., Tecchiato, V., Di Stefano, F., et al. (2018). An integrated P-T-H 2 O-lattice strain model to quantify the role of clinopyroxene fractionation on REE+ Y and HFSE patterns of mafic alkaline magmas: Application to eruptions at Mt. Etna. *Earth-Science Reviews*, *185*, 32–56. <https://doi.org/10.1016/j.earscirev.2018.05.014>
- Mollo, S., Del Gaudio, P., Ventura, G., Iezzi, G., & Scarlato, P. (2010). Dependence of clinopyroxene composition on cooling rate in basaltic magmas: Implications for thermobarometry. *Lithos*, *118*(3-4), 302–312. <https://doi.org/10.1016/j.lithos.2010.05.006>
- Mollo, S., Iezzi, G., Ventura, G., Cavallo, A., & Scarlato, P. (2012). Heterogeneous nucleation mechanisms and formation of metastable phase assemblages induced by different crystalline seeds in a rapidly cooled andesitic melt. *Journal of non-crystalline solids*, *358*(12-13), 1624–1628. <https://doi.org/10.1016/j.jnoncrysol.2012.04.010>
- Mollo, S., Lanzafame, G., Masotta, M., Iezzi, G., Ferlito, C., & Scarlato, P. (2011). Cooling history of a dike as revealed by mineral chemistry: A case study from Mt. Etna volcano. *Chemical Geology*, *288*(1-2), 39–52. <https://doi.org/10.1016/j.chemgeo.2011.06.016>
- Moore, H. J., Arthur, D. W. G., & Schaber, G. G. (1978). Yield strengths of flows on the Earth, Mars, and Moon. In *Lunar and Planetary Science Conference Proceedings*, (Vol. 9, pp. 3351–3378).
- Morgavi, D., Petrelli, M., Vetere, F. P., González-García, D., & Perugini, D. (2015). High-temperature apparatus for chaotic mixing of natural silicate melts. *Review of Scientific Instruments*, *86*(10), 105108. <https://doi.org/10.1063/1.4932610>
- Morrison, A. A., Zanetti, M., Hamilton, C. W., Lev, E., Neish, C. D., & Whittington, A. G. (2019). Rheological investigation of lunar highland and mare impact melt simulants. *Icarus*, *317*, 307–323. <https://doi.org/10.1016/j.icarus.2018.08.001>
- Mouginis-Mark, P. J., Wilson, L., Head, J. W., Brown, S. H., Hall, J. L., & Sullivan, K. D. (1984). Elysium Planitia, Mars: Regional geology, volcanology, and evidence for volcano-ground ice interactions. *Earth, Moon, and Planets*, *30*(2), 149–173. <https://doi.org/10.1007/BF00114309>
- Murri, M., Cámara, F., Adam, J., Domeneghetti, M. C., & Alvaro, M. (2018). Intracrystalline “geothermometry” assessed on clinopyroxene bearing synthetic rocks. *Geochimica et Cosmochimica Acta*, *227*, 133–142. <https://doi.org/10.1016/j.gca.2018.02.010>
- Murri, M., Scandolo, L., Fioretti, A. M., Nestola, F., Domeneghetti, M. C., & Alvaro, M. (2016). The role of Fe content on the Fe-Mg exchange reaction in augite. *American Mineralogist*, *101*(12), 2747–2750. <https://doi.org/10.2138/am-2016-5717>

- Mysen, B., & Richet, P. (2005). Iron-bearing melts. In *Silicate glasses and melt*, chap. 10, (pp. 291–327). Amsterdam, Netherlands: Elsevier Sci.
- Mysen, B. O., Virgo, D., & Seifert, F. A. (1982). The structure of silicate melts: Implications for chemical and physical properties of natural magma. *Reviews of Geophysics*, *20*(3), 353–383. <https://doi.org/10.1029/RG020i003p00353>
- Ochs, F. A., & Lange, R. A. (1999). The density of hydrous magmatic liquids. *Science*, *283*(5406), 1314–1317. <https://doi.org/10.1126/science.283.5406.1314>
- Parfitt, E. A., & Wilson, L. (2008). *The role of volatiles. Fundamentals of physical volcanology*, (pp. 64–76).
- Petrelli, M., El Omari, K., Le Guer, Y., & Perugini, D. (2016). Effects of chaotic advection on the timescales of cooling and crystallization of magma bodies at mid crustal levels. *Geochemistry, Geophysics, Geosystems*, *17*, 425–441. <https://doi.org/10.1002/2015GC006109>
- Pistone, M., Caricchi, L., Ulmer, P., Burlini, L., Ardia, P., Reusser, E., et al. (2012). Deformation experiments of bubble-and crystal-bearing magmas: Rheological and microstructural analysis. *Journal of Geophysical Research*, *117*, B05208. <https://doi.org/10.1029/2011JB008986>
- Rossi, S., Petrelli, M., Morgavi, D., González-García, D., Fischer, L. A., Vetere, F., & Perugini, D. (2017). Exponential decay of concentration variance during magma mixing: Robustness of a volcanic chronometer and implications for the homogenization of chemical heterogeneities in magmatic systems. *Lithos*, *286–287*, 396–407. <https://doi.org/10.1016/j.lithos.2017.06.022>
- Ryerson, F. J., Weed, H. C., & Piwinski, A. J. (1988). Rheology of subliquidus magmas: 1. Picritic compositions. *Journal of Geophysical Research*, *93*(B4), 3421–3436. <https://doi.org/10.1029/JB093iB04p03421>
- Sato, H. (2005). Viscosity measurement of subliquidus magmas: 1707 basalt of Fuji volcano. *Journal of Mineralogical and Petrological Sciences*, *100*(4), 133–142. <https://doi.org/10.2465/jmps.100.133>
- Schuessler, J. A., Botcharnikov, R. E., Behrens, H., Misiti, V., & Freda, C. (2008). Amorphous materials: Properties, structure, and durability: Oxidation state of iron in hydrous phono-tephritic melts. *American Mineralogist*, *93*(10), 1493–1504. <https://doi.org/10.2138/am.2008.2795>
- Sehlke, A., & Whittington, A. G. (2015). Rheology of lava flows on Mercury: An analog experimental study. *Journal of Geophysical Research: Planets*, *120*, 1924–1955. <https://doi.org/10.1002/2015JE004792>
- Sehlke, A., & Whittington, A. G. (2016). The viscosity of planetary tholeiitic melts: A configurational entropy model. *Geochimica et Cosmochimica Acta*, *191*, 277–299. <https://doi.org/10.1016/j.gca.2016.07.027>
- Shirey, S. B., 1997, Initial Os isotopic compositions of Munro Township, Ontario, komatiites revisited: Additional evidence for near-chondritic, late-Archean convecting mantle beneath the Superior Province, in Abstracts of the 7th Goldschmidt Conference: LPI Contribution 921, Abstract 2375.
- Smith, P. M., & Asimow, P. D. (2005). Adibat\_1ph: A new public front-end to the MELTS, pMELTS, and pHMELTS models. *Geochemistry, Geophysics, Geosystems*, *6*, Q02004. <https://doi.org/10.1029/2004GC000816>
- Soldati, A., Sehlke, A., Chigna, G., & Whittington, A. (2016). Field and experimental constraints on the rheology of arc basaltic lavas: The January 2014 eruption of Pacaya (Guatemala). *Bulletin of Volcanology*, *78*(6), 43. <https://doi.org/10.1007/s00445-016-1031-6>
- Spera, F. J., Borgia, A., Strimple, J., & Feigenson, M. (1988). Rheology of melts and magmatic suspensions: 1. Design and calibration of concentric cylinder viscometer with application to rhyolitic magma. *Journal of Geophysical Research*, *93*(B9), 10,273–10,294. <https://doi.org/10.1029/JB093iB09p10273>
- Spina, L., Scheu, B., Cimarelli, C., Arciniega-Ceballos, A., & Dingwell, D. B. (2016). Time scales of foam stability in shallow conduits: Insights from analogue experiments. *Geochemistry, Geophysics, Geosystems*, *17*, 4179–4194. <https://doi.org/10.1002/2016GC006455>
- Stixrude, L., & Lithgow-Bertelloni, C. (2011). Thermodynamics of mantle minerals—II. Phase equilibria. *Geophysical Journal International*, *184*(3), 1180–1213. <https://doi.org/10.1111/j.1365-246X.2010.04890.x>
- Udry, A., & Day, J. M. D. (2018). 1.34 billion-year-old magmatism on Mars evaluated from the co-genetic nakhlite and chassignite meteorites. *Geochimica et Cosmochimica Acta*, *238*, 292–315. <https://doi.org/10.1016/j.gca.2018.07.006>
- Vaucher, J., Baratoux, D., Toplis, M. J., Pinet, P., Mangold, N., & Kurita, K. (2009). The morphologies of volcanic landforms at Central Elysium Planitia: Evidence for recent and fluid lavas on Mars. *Icarus*, *200*(1), 39–51. <https://doi.org/10.1016/j.icarus.2008.11.005>
- Vetere, F., Behrens, H., Botcharnikov, R., Holtz, F., & Fanara, S. (2014). The role of alkalis in the solubility of H<sub>2</sub>O and CO<sub>2</sub> in silicate melts. Implication for phonotephritic magmas. *Contribution to Mineralogy and Petrology*, *167*(5), 1014. <https://doi.org/10.1007/s00410-014-1014-6>
- Vetere, F., Behrens, H., Holtz, F., & Neuville, D. R. (2006). Viscosity of andesitic melts—New experimental data and a revised calculation model. *Chemical Geology*, *228*(4), 233–245. <https://doi.org/10.1016/j.chemgeo.2005.10.009>
- Vetere, F., Jezi, G., Behrens, H., Holtz, F., Ventura, G., Misiti, V., et al. (2015). Glass forming ability and crystallisation behaviour of sub-alkaline silicate melts. *Earth-Science Reviews*, *150*, 25–44. <https://doi.org/10.1016/j.earscirev.2015.07.001>
- Vetere, F., Rossi, S., Namur, O., Morgavi, D., Misiti, V., Mancinelli, P., et al. (2017). Experimental constraints on the rheology, eruption, and emplacement dynamics of analog lavas comparable to Mercury's northern volcanic plains. *Journal of Geophysical Research: Planets*, *122*, 1522–1538. <https://doi.org/10.1002/2016JE005181>
- Vetere, F., Sato, H., Ishibashi, H., De Rosa, R., & Donato, P. (2013). Viscosity changes during crystallization of a shoshonitic magma: New insights on lava flow emplacement. *Journal of Mineralogical and Petrological Sciences*, *108*(3), 144–160. <https://doi.org/10.2465/jmps.120724>
- Vogel, H. (1921). The law of the relation between the viscosity of liquids and the temperature. *Physikalische Zeitschrift*, *22*, 645–646.
- Vona, A., & Romano, C. (2013). The effects of undercooling and deformation rates on the crystallization kinetics of Stromboli and Etna basalts. *Contributions to Mineralogy and Petrology*, *166*(2), 491–509. <https://doi.org/10.1007/s00410-013-0887-0>
- Vona, A., Romano, C., Dingwell, D. B., & Giordano, D. (2011). The rheology of crystal-bearing basaltic magmas from Stromboli and Etna. *Geochimica et Cosmochimica Acta*, *75*(11), 3214–3236. <https://doi.org/10.1016/j.gca.2011.03.031>
- Williams, D. A., Kerr, R. C., Leshner, C. M., & Barnes, S. J. (2001). Analytical/numerical modeling of komatiite lava emplacement and thermal erosion at Perseverance, Western Australia. *Journal of Volcanology and Geothermal Research*, *110*(1–2), 27–55. [https://doi.org/10.1016/S0377-0273\(01\)00206-2](https://doi.org/10.1016/S0377-0273(01)00206-2)
- Wilson, L., & Head, J. W. (1994). Mars: Review and analysis of volcanic eruption theory and relationships to observed landforms. *Reviews of Geophysics*, *32*(3), 221–263. <https://doi.org/10.1029/94RG01113>
- Wilson, L., Mougins-Mark, P. J., Tyson, S., Mackown, J., & Garbeil, H. (2009). Fissure eruptions in Tharsis, Mars: Implications for eruption conditions and magma sources. *Journal of Volcanology and Geothermal Research*, *185*(1–2), 28–46. <https://doi.org/10.1016/j.jvolgeores.2009.03.006>